PHOTOLUMINESCENT ZINC SULFIDE OPTICAL CERAMICS

BY

YIYU LI

A THESIS
SUBMITTED TO THE FACULTY OF

ALFRED UNIVERSITY

IN PARTIAL FULFILLMENT OF THE REQUIREMENTS
FOR THE DEGREE OF

MASTER OF SCIENCE

IN

CERAMIC ENGINEERING

ALFRED, NEW YORK

MAY, 2015

PHOTOLUMINESCENT ZINC SULFIDE OPTICAL CERAMICS

BY

YIYU LI

B.S. CENTRAL SOUTH UNIVERSITY (2010)

SIGNATURE OF AUTHOR_____

APPROVED BY _____
YIQUAN WU, ADVISOR

_____
S.K SUNDARAM, ADVISORY COMMITTEE

_____
DAWEI LIU, ADVISORY COMMITTEE

_____
CHAIR, ORAL THESIS DEFENSE

ACCEPTED BY_____
DOREEN D. EDWARDS, DEAN
KAZUO INAMORI SCHOOL OF ENGINEERING

ACKNOWLEDGMENTS

I would like to first and foremost, to express my sincere and earnest gratitude to my adviser, Dr. Yiquan Wu, for his support and help during my study and living at Alfred. His learned knowledge on science and great passion on research always encouraged me to motivate myself to dedicate to research work. I would also like to thank my committee members, Dr. S.K. Sundaram and Dr. Dawei Liu, for their valuable advice on my thesis work.

My gratitude also goes to Slawomir Zdzieszynski, Gerry Wynick, Francis Williams, Terry Guild and Dr. Mirela Dragan for their great technical help on my experiments. In addition, I am very indebted to my colleagues and friends at Alfred, Yin Liu, Yan Yang, Sureeporn Chothirawat, Bo Zhang, Wei Zhang, Peng Gao, Yuxuan Gong, Dimple Pradhan, Trevyn Hey, Peter Metz, Yiming Li and Thomas Olson for their priceless help on my research and life.

At last, I would like to express my special thanks to my family for their care, encouragement, understanding and endless love to me.

TABLE OF CONTENTS

LIST OF TABLES

Page

LIST OF FIGURES

Page

ABSTRACT

Zinc sulfide is an attractive infrared (IR) optical ceramic material due to its desirable IR transmittance in the wavelength range of 8-12 μm. In this research, studies on the synthesis of ZnS powders and consolidation of ZnS ceramics were performed to understand the correlation between processing and property of ZnS optical ceramics. The photoluminescence characteristics of ZnS optical ceramics were also studied to provide rational discussions and interpretations of the phenomena.

Four ZnS powders were synthesized via different wet chemical precipitation routes. Phase composition and microstructure analyses presented that they had pure cubic ZnS phases and finer particles with higher specific surface energy, compared with the commercial ZnS powders. In addition, it was found that the hot water bath route could contribute to slow and homogenous particle growth, resulting in synthesis of ZnS homogenous spherical particles. Second, the synthesized and commercial ZnS powders were consolidated by field assisted sintering technique (FAST) and vacuum hot pressing (VHP), respectively. It was revealed that the ZnS ceramics sintered by using the synthesized powders with homogenous particles had better densification and more desirable optical properties. Additionally, VHP was considered to be a more suitable sintering method to fabricate ZnS optical ceramics, due to the more sufficient densification and less carbon contamination. At last, the photoluminescence properties of the as-sintered undoped ZnS optical ceramics were measured. It was found that the blue emission was derived from the transfer of electrons from zinc vacancies to conduction band, and the green photoluminescence of the ZnS optical ceramics was due to the electron transfer in sulfur defects associated with elemental sulfur species. The increase of the green luminescence lifetime was attributed to processing conditions.

INTRODUCTION

A. Optical Ceramics

1. Development of Optical Ceramics

Optical ceramics refer to the ceramics used in optical applications, especially to optically transparent or translucent polycrystalline ceramics. It is well acknowledged that light is a form of electromagnetic radiation. When light proceeds from a medium into another one, some light will be absorbed, some will be reflected at the interface between the two media, and some will be transmitted through the medium.[1] Different materials will react differently with light based on the basic bonding characteristics of various materials. Materials that are capable of transmitting light with relatively little absorption and reflection are transparent materials. Usually, beyond low light absorption and reflection, low scattering loss is also imperative for clear optical transparency.[2,3]

Conventionally, optically transparent materials include polymers and noncrystalline ceramic (glass) materials. However, theses materials usually have poor mechanical strengths and undesirable chemical and physical stabilities, which seriously limit their applications in harsh environments. In addition, due to the low decomposition temperature of the polymers and glasses, it is not feasible for them to be used for any transparent materials applications at high temperatures. Moreover, the low transmittance in the IR wavelength range also affects the variety of their applications. With the rapid development and advancement of materials science and engineering, single crystals for some materials were developed and studied. Since single crystals are highly perfect without any pores and defects, which results in their transparency, they are attractive candidates for the transparent materials applications. Additionally, desirable mechanical properties combined with stable physiochemical properties and thermal stabilities of single crystals almost dispel the concerns for the traditional transparent materials. Nevertheless, single crystal growth needs very

complicated and expensive facilities, rendering the fabrication of single crystals to be costly. The growth of single crystal is also time-consuming, and difficult for production of large volumes and complicated shapes. Additionally, when it comes to single crystals for solid-state laser gain media applications, the concentration and homogeneity of laser active ions are limited by single crystals. Compared with single crystals, optical ceramics or transparent ceramics are demonstrated to own the merits of cost-effectiveness, large-volume production, viability of shape controlling, and better mechanical properties. They can also enable the dopants to be incorporated heavily and homogeneously. Thus, optical ceramics have emerged as promising candidates for transparent materials with expanded range capabilities. They are widely used in solid-stare lasers, scintillators, lighting, armors, domes, optical systems and transparent electro-optic ceramic devices.[2]

2. Materials for Optical Ceramics

It is well acknowledged that polycrystalline ceramics have grains and grain boundaries. Thus, grain boundaries, residual pores, defects, and second phases within ceramics can all serve as sources of optical scattering, which in turn affect the transparency of ceramics. In addition, when light travels through polycrystalline ceramic materials with different crystal structures, additional scattering loss will occur to the ceramics with anisotropic structure due to the inherent birefringence at grain boundaries.[4] Figure 1 shows the different responses for materials with anisotropic and isotropic crystal structures when light travels through. This birefringence will affect the optical performance of ceramics and limit the applications as optical elements. Therefore, most currently reported and studied optical ceramics have the optically isotropic cubic crystal structure with no birefringence. However, some of the anisotropic ceramics can also be transparent only when the birefringence can be minimized or avoided. One way to minimizing the scattering loss by inherent birefringence is to keep the grain size small (with the reference to the wavelength) such as nanostructured ceramics. The other demonstrated way is to align the grains so that their refractive indexes match along a single direction.[5] As a result, with the

development of ceramic science and technology, some materials with anisotropic crystal structure are also capable of serving as optical ceramics.

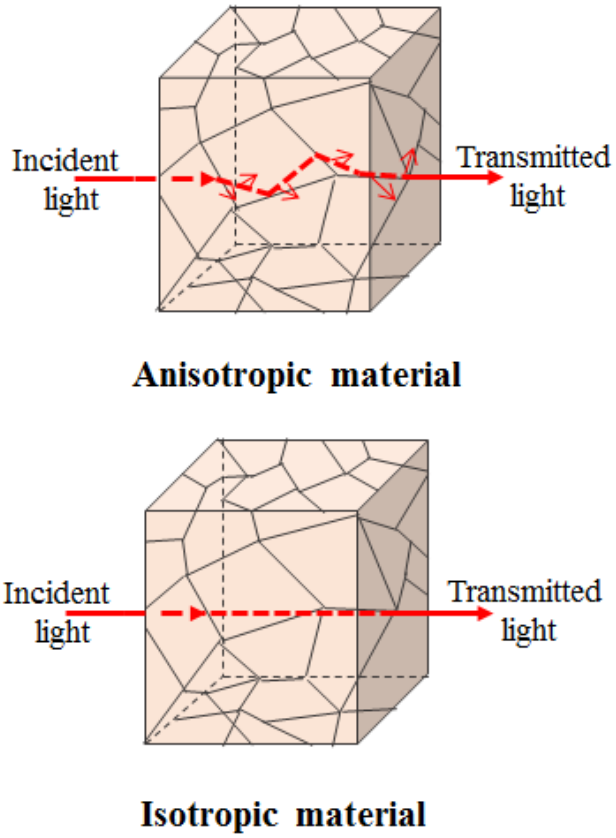

Figure 1. Diagram of different responses for materials with anisotropic and isotropic crystal structures when light travels through.[5]

As one of the widely applied optical ceramics, yttrium aluminum garnet (YAG, $Y_3Al_5O_{12}$) is a synthetic crystalline material with cubic garnet structure. Since YAG is a desirable host to the rare earth elements (Nd, Tm, Er, Cr and Yb), which can be doped into YAG lattice as laser activator ions, YAG optical ceramics have been extensively used in high power solid state lasers applications for various lasers with different excitation wavelength. In addition, the Ce-doped YAG optical ceramics can be employed as scintillators, and YAG ceramics are also well known for their applications are IR transparent windows and envelopes in lamps. Since A. Ikesue *et al.* first reported the transparent optical polycrystalline YAG ceramics by a solid-state reaction method combined with vacuum sintering,[6] different powder syntheses,

forming approaches and sintering techniques are applied to fabrications of YAG ceramics. It was reported by the R. Chaim *et al.* that highly transparent YAG optical ceramics could be obtained by spark plasma sintering at lower temperatures in shorter dwell times.[7] S.H. Lee *et al.* proved that solid-state reactive sintering by adding tetraethyl orthosilicate as the sintering additive was capable of processing optical Nd:YAG ceramics, which have similar performance to the single crystals as laser materials.[8] By taking advantage of sol-gel method to synthesize YAG powder, T. Tachiwaki *et al.* prepared YAG optical ceramics via vacuum sintering without any sintering additives.[9]

Magnesium aluminate spinel ($MgAl_2O_4$) is one of typical representatives in the cubic spinel family. Due to its excellent optical performance, desirable mechanical strength, and favorable thermal stability, $MgAl_2O_4$ optical ceramics have attracted a lot of interest and they are extensively used in transparent windows and lenses applications. Since it is difficult to prepare $MgAl_2O_4$ optical ceramics by high purity raw precursors via conventional sintering, the pressure-assisted sintering techniques are usually applied. I. E. Reimanis *et al*. proposed a three-step and single pot process to synthesized $MgAl_2O_4$ powder, and succeeded in fabricating $MgAl_2O_4$ optical ceramics via hot pressing by adding LiF as the sintering additive.[10] It is reported by K. Morita *et al*. that $MgAl_2O_4$ optical ceramics with high strength could be achieved by spark plasma sintering at a lower heating rate.[11] By applying ultra high pressure during the sintering process, $MgAl_2O_4$ optical ceramics were demonstrated to be obtained at lower temperatures.[12]

As a material for IR optical windows and high temperature optical ceramics, MgO also has the cubic crystal structure as halite. It is proposed that the MgO transparent ceramics can be fabricated by hot pressing or spark plasma sintering at low temperatures by adding sintering additives.[13] R. Chaim *et al*. suggested an approach to fabricate fully dense MgO optical ceramics by using rapid and lower temperature spark plasma sintering.[14]

With excellent chemical and physical properties, yittria (Y_2O_3) optical ceramics possessing the cubic bixbyite structure are promising candidates for application in lasers, lighting industries, armors, IR windows and scintillators. Early in 1969, S.K. Dutta *et al*. developed the optically transparent Y_2O_3 ceramics by vacuum hot pressing.[15] D. Huo *et al*. investigated the rheology behaviors of the Y_2O_3 slurry and made optical Y_2O_3 ceramics by slip casting followed by vacuum sintering.[16] Due to the potential application as IR transparent optical ceramics for both Y_2O_3 and MgO,[17] S. Wu *et al*. adopted sol-gel combustion to synthesize the composite powders and developed Y_2O_3-MgO composite optical ceramics via hot pressing.[18]

Aluminium oxynitride (AlON, $Al_{23}O_{27}N_5$) is an important optical ceramic material used in extensive range of applications from IR windows and lenses to transparent armors, due its desirable optical properties combined with excellent mechanical properties. It also has the birefringence-free cubic crystal structure with isotropic optical and mechanical properties. Different powder syntheses followed by diverse sintering methods including conventional pressureless sintering and novel sintering techniques are applied to the fabrication of AlON optical ceramics.[19] By using Y_2O_3 as the sintering aid, J. Cheng *et al.* developed fully optically transparent AlON ceramics via microwave reactive sintering.[20] F.C. Sahin *et al.* demonstrated the feasibility of preparing AlON optical ceramics by taking advantage of spark plasma sintering for both reaction and sintering.[21]

Although zirconia (ZrO_2) owns the monoclinic structure at room temperature, and experience reversible phase transitions to tetragonal and then to cubic phase at elevated temperatures, yittria can be incorporated into ZrO_2 lattice to enable the stability of the cubic crystal structure at room temperature which is so-called yittria-stabilized zirconia (YSZ). The YSZ optical ceramics can be used in optical lens systems.[22] U. Peuchert *et al.* reported the fabrication of YSZ optical ceramics reaching 68% in maximum transmittance with a thickness of 5.6 mm, through a combined process of vacuum sintering and hot isostatic pressing by adopting titania as the sintering aid.[23]

Owing to the combination of high transparency and excellent electro-optic property, (Pb,La)(Zr,Ti)O_3 (PLZT) and Pb($Mg_{1/3}Nb_{2/3}$)O_3-$PbTiO_3$ (PMN-PT) optical ceramics with the cubic perovskite structure have been widely used in electro-optic devices. J. Huang pointed out that commercial PLZT and PMN-PT optical ceramics could be prepared by using chemical precipitation to synthesize high purity powders and uniaxial hot pressing for densification.[24] Meanwhile, W. Ruan *et al.* employed a two-stage sintering method to fabricate the PMN-PT optical ceramics with high electro-optic effect by adding PbO as the sintering aid.[25]

Alpha-Alumina (α-Al_2O_3) ceramics are the most typical representatives of optical ceramics with anisotropic structure. They are extensively applied in transparent armors, envelopes of lamps and electromagnetic windows, due to their supreme mechanical properties.[26] Commonly, the highly consolidated α-Al_2O_3 optical ceramics can only be translucent. However, as discussed previously, it is viable to prepare optical ceramics with anisotropic structures by reducing the grain size or orientation of the grains in order to reduce the effect of birefringence. Through modification of processes such as Al_2O_3 precursor powder synthesis, green body forming and sintering, the optical and mechanical properties can be dramatically improved. K. Hayashi *et al.* prepared Al_2O_3 optical ceramics with high in-line optical transmittance via injection molding followed by hot isostatic pressing, and found that decreasing the grain size could result in improvement of the optical properties.[27] By using a magnetic field to align the grains during the slip casting process, X. Mao et al. succeeded in obtaining Al_2O_3 optical ceramics with high transmittance.[28] In addition, a light scattering model based on geometrical optics was derived to describe optical transmittance performance of the fully dense polycrystalline Al_2O_3 under birefringence effect, in order to provide a reference for improving optical properties of Al_2O_3 ceramics.[29] As a promising candidate for solid-state gain media, Nd or Yb doped strontium fluoride phosphate ($Sr_5F(PO_4)_3$, S-FAP) optical ceramics have attracted a lot of attention, It was recently reported by Y. Wu *et al.* that the optically transparent Yb:S-FAP (hexagonal crystal structure) nanocrystalline ceramics could be

processed via spark plasma sintering (SPS) with nanopowder prepared via a co-precipitation method.[30] Table I shows physical properties of the typical optical ceramics materials proving the favorable properties of the optical ceramics.

Table I. Physical Properties of the Typical Optical Ceramic Materials[31]

Material	Strength (MPa)	Knoop hardness (Kg/mm^2)	Modulus (GPa)	Density (g/cm^3)	Melting point (K)
AlON	300	1950	323	3.68	2425
Al_2O_3	700	1500-2200	345-386	3.98	2300
Y_2O_3	150	720	174	5.03	2430
$MgAl_2O_4$	100-200	1400	273	3.58	2400
YAG	200-250	1215	300	4.55	1950
ZrO_2	210	1100	180-200	6.52	2128

Besides the above oxide materials for optical ceramics, CaF_2 and ZnS with cubic crystal structure are promising candidates for the optical ceramics applications in the mid-IR wavelength due to their wider transparency wavelength range. The rare earth elements doped CaF_2 optical ceramics can be used in laser applications. For instance, it was reported by Z. Liu *et al.* that the Er doped CaF_2 optical ceramics could be prepared by vacuum hot pressing to have good optical performance.[32]

3. Processing of Optical Ceramics

The light transmittance is one of the most significant optical properties for transparent polycrystalline ceramics and also a vital factor relative to the ultimate in-service application. It is mentioned that the absorption, reflection and scattering are closely related to the optical transmittance of materials. In order to achieve optical transparency, the scattering within optical polycrystalline ceramics needs to be avoided and eliminated. Ceramics from fine powders generally result in finely grained

polycrystalline ceramics. The natural characteristics of ceramics contribute to diverse scattering sources of light. Figure 2 shows a schematic of scattering sources within polycrystalline ceramics. The different compositions between grains and grain boundaries can lead to scatterings of light. Due to the dramatic difference in refractive index between pores and ceramics, residual pores between grains and grain boundaries are the most important factors to affect optical properties. They can effectively scatter light and make ceramics opaque. In addition, the presence of second phases and inclusion with different refractive indexes can lead to the light scattering as well. Besides, known as birefringence, the double refraction from materials with anisotropic crystal structure is also a factor to scatter light. The physical factors such as thickness and surface roughness also affect the optical properties.

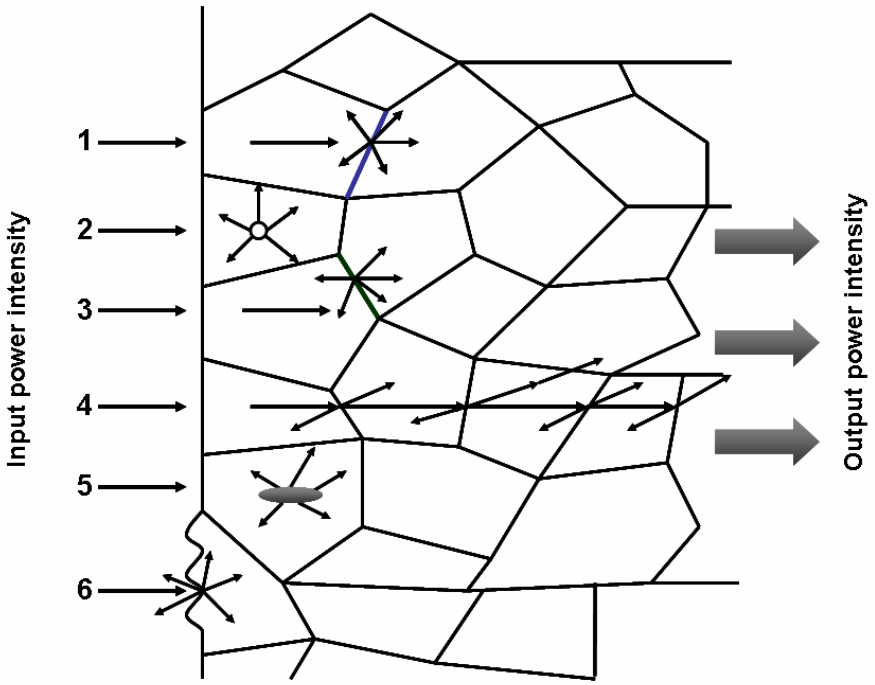

Figure 2. Schematic showing the microstructure of conventional transparent optical ceramics, light scattering and the attenuation of input power through the ceramic body. Strong scattering owing to (1) grain boundary, (2) residual pores, (3) secondary phase, (4) double refraction, (5) inclusions and (6) surface roughness in ceramics prohibits applications in optics.[33]

Processing of optical ceramics plays an extremely important role in minimizing and eliminating the scatterings of light within ceramics. It usually includes synthesis of raw powders, forming, sintering and post-treatment. Optimization of the processing methods have been studied and performed to obtain optical ceramics with higher performance. Among all the procedures, powder synthesis and ceramics consolidation are the most important because they correlate closely to optical performance of optical ceramics by deceasing light scattering sources. As discussed earlier, second phases and impurities can affect the optical transmittance of ceramics. Therefore, it is necessary to synthesize raw powders with high purity to avoid contamination from impurities. Additionally, the microstructure and morphology of the raw powders are of significance to consolidation of the ceramics. Raw powders with favorable sintering properties can aid in the densification and pores removal during the sintering process, which leads to the fabrication of dense ceramics. Tremendous studies on various synthetic methods such as solid-state reaction, co-precipitation, sol-gel method and flame spray pyrolysis have been performed to synthesize raw powders to fabricate optical ceramics. It is noted that, compared with the traditionally used solid-state reaction method, wet chemistry methods have the advantages of synthesizing powders with smaller particle size, finer morphology, and better sintering properties, which in turns render it to attract a lot of attention as a promising powder synthesis approach for optical ceramics.

In addition to the raw powder synthesis, the sintering process is another important factor contributing to the optical performance of optical ceramics. Through grain growth and grain boundary diffusion during the sintering stages, pores can be eliminated, and ceramics can be consolidated. Because of the demands of high densification and low porosity for optical ceramics, different from the traditional sintering process, the one for optical ceramics fabrication often needs some external conditions such as pressure and atmosphere, in order to achieve more desirable optical properties. Hot pressing, vacuum sintering, vacuum hot pressing, hot isostatic pressing (HIP), and SPS are the commonly applied sintering techniques for

consolidation of optical ceramics. By simultaneous application of pressure and heat, hot pressing can facilitate particle rearrangement and particle flow between particles. Usually, a uniaxial pressure is loaded on ceramics at elevated temperatures during sintering, which contributes to pores removal. Vacuum sintering is the sintering process operated in vacuum, and the vacuum condition can provide an additional driving force for densification. The combination of hot pressing and vacuum sintering leads to the vacuum hot pressing, which recently becomes a promising alternative to prepare optical ceramics. Different from the applied uniaxial pressure, HIP employed a gas isostatic pressure providing pressure from all directions for further densification. The approach by combining HIP with other sintering methods is a common way to fabricate optical ceramics. SPS, also known as field assisted sintering technique (FAST), is a newly developed sintering technique for short sintering time.[34] By heating samples using a pulse direct current under high pressure to facilitate the mass transport, this method can lower sintering temperatures, curb grain growth and achieve enhanced densification compared with conventional sintering methods.

B. Introduction of ZnS

1. Fundamental Properties of ZnS

As one of the firstly discovered semiconductors, zinc sulfide has been extensively studied and researched for a long time due to its unique physical and chemical properties. It is widely acknowledged that ZnS is a semiconductor with a wide band gap and can be employed in various applications, such as photoluminescence, electroluminescence, thermoluminescence, IR lenses and windows, optical elements, sensors, and photocatalysis.

Natural ZnS forms include two well-characterized crystal structures, which are sphalerite (zinc blende) and wurtzite. In addition, it was also demonstrated through experiments that ZnS transformed to rocksalt under pressures of 15.0-24.5 GPa.[35-38] Figure 3 shows the two most extensively studied crystal structures of ZnS. Figure 4 shows the difference of dihedral conformation and stacking for the two structures.

Zinc blende belonging to the cubic space group F-43m is the prototype of B-3 structure, while wurtzite belonging to the hexagonal space group $P6_3mc$ is the prototype of B-4 Structure. The two crystal structures of ZnS are both close-packed structures with an atomic packing factor of 0.74. The zinc atoms and sulfur atoms are tetrahedrally coordinated with a coordination number of 4 for both phases. However, the atoms stacking patterns are different. The ZnS sphalerite possesses the close-packed atomic arrangement as ABCABC stacking pattern on the {110} planes along [111] axis, while the ZnS wurtzite has close-packed atomic arrangement as ABABAB stacking pattern on the {0001} planes along $[1\bar{1}20]$ axis. Since the two structures are very similar, the ZnS sphalerite and wurtzite can often transform to each other. For the ZnS bulks, the low temperature sphalerite phase undergoes a phase transition to wurtzite at 1020 ºC. However, through decreasing the particle size and tuning the morphology of ZnS by nanotechnology, researchers are capable of lowering the effective phase transformation temperature.

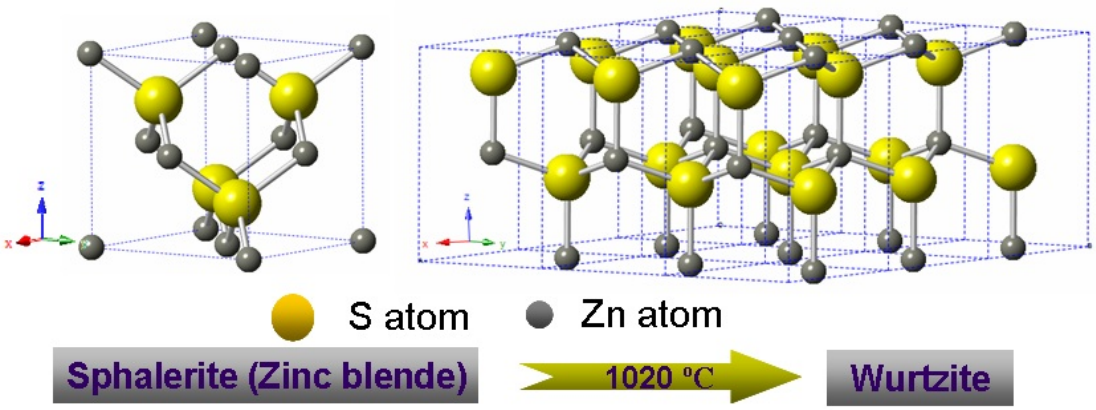

Figure 3. Two well-characterized crystal structures of ZnS.

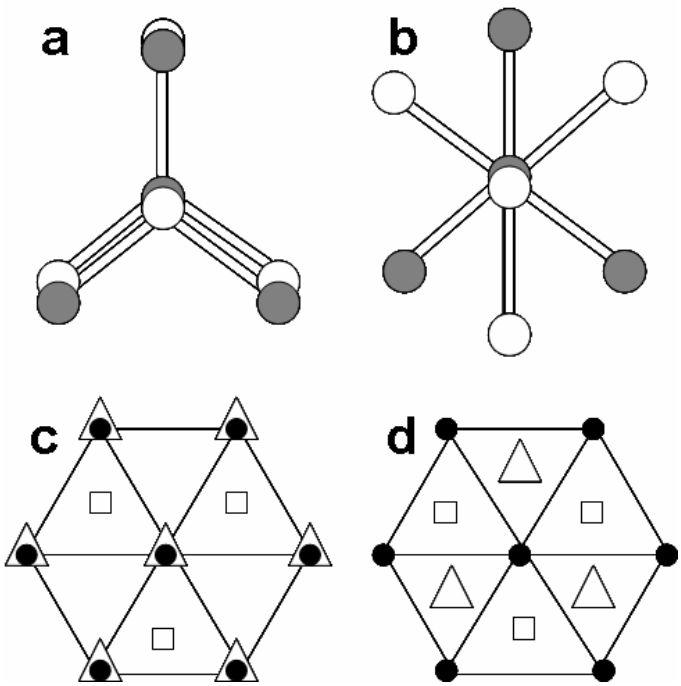

Figure 4. (a) and (b) show the "eclipsed" and "staggered" dihedral conformations for wurtzite and sphalerite, respectively. (c) and (d) show the layer stacking along [111] axis.[39]

The trivial difference in ZnS two main crystal structures leads to difference in optical and electronic properties, which results in different application for the two structures of ZnS. Experiments and simulations indicate the two phases of ZnS are both semiconductors with direct band gaps. The ZnS sphalerite phase has a band gap of 3.72 eV, while wurtzite has a higher band gap as 3.77 eV.[40] It is considered that the band structure of wurtzite can be regarded as a disturbance of the cubic crystal field, which introduces more valence and conduction bands due to the reduction of symmetry for hexagonal wurtzite. Owing to different defects and dopants in ZnS host lattice, ZnS can serve as both p-type and n-type semiconductors. As can be seen from the space groups the two phases belong to, they both posses the intrinsic asymmetric nature, resulting the piezoelectricity from mechanical tension and compression. Additionally, different from sphalerite, wurtzite has a single permanent polar axis along c-axis, which in turn leads to the pyroelectricity. The piezoelectric characteristics of ZnS nanobelts enable them to be employed in diverse sensing

applications such as nanocantilevers with increased sensitivity in scanning probe microscopy.[41]

In bulk form at ambient pressure, ZnS goes through a phase transition at 1020 ºC from the low-temperature cubic sphalerite phase to the hexagonal wurtzite phase.[42] In terms of the properties desired for both electronic and optoelectronic applications, wurtzite is a more attractive phase than sphalerite due to its wider intrinsic band gap. Thus, in applications where wurtzite is the desired phase, its stability can be increased by decreasing particle size to the nanometer scale, which lowers the effective transition temperature of the ZnS. In addition, surface area and morphology can be tuned to promote the formation of the wurtzite during syntheses.[43-46] However, for IR optical ceramics applications, cubic sphalerite is preferred, as it is optically isotropic. The presence of wurtzite in primarily sphalerite ZnS reduces transparency due to the anisotropic nature of the hexagonal structure of wurtzite. Currently, chemical vapor deposition (CVD) combined with HIP is the mostly employed approach to prepare ZnS IR optical ceramics at lower temperatures to prevent the phase transition. Additionally, it has also been demonstrated that under an applied uniaxial pressure, ZnS ceramics can be densified at lower temperatures during hot pressing, which improves optical properties through reduction of the formation of wurtzite phase which occurs at higher sintering temperatures.[47,48]

2. Nanostructured ZnS

Diverse facile approaches have been adopted to fabricate ZnS with nanostructures including 0- 1- and 2-dimensions. Research on nanostructured ZnS with different morphologies is extensively performed to understand the relationship between processing and properties.[40] It is known that quantum dots refer to semiconductor nanoparticles with enhanced optical and electric performances due to the quantum size effect induced by decreasing of the particle size into nanoscale. Thus, 0-dimention ZnS nanocrystals are also named ZnS quantum dots, which are widely used in electronic, optoelectronic, and photocatalyst applications. The synthesis

methods based on solution chemistry are the main approaches to prepare the 0-dimension ZnS nanocrystals. In addition, the current technology can tune and control the structure of 0-dimension ZnS to be core/shell structure or hollow structure, with higher specific surface area and enhanced luminescence efficiency. Due to the similarity with ZnO in band gap to semiconductors, nanostructured ZnS with 1-dimension such as nanowires, nanorods, and nanotubes have also been extensively studied for their potential applications in optics, electronics and sensors. Various synthetic methods including vapor-phase and solution-based syntheses were adopted to fabricate grow 1-dimension ZnS materials. As the typical representative of the 2-dimension nanostructured ZnS, ZnS thin films have seen fabricated by diverse synthesis methods including deposition methods, epitaxy methods, sol-gel and spray pyrolysis. They have been widely used in light emitting diodes, reflector and dielectric filters.

3. ZnS IR Optical Ceramics

The IR optical ceramics can be divided into two groups. One is the wavelength range of 3-5 μm and the other is from 8-12 μm. The IR transparent ceramics in 3-5 μm range can be used as IR windows or domes for the protecting of detectors for IR guided missiles. A lot of aforementioned oxides for optical ceramics can be applied as IR optical ceramics in 3-5 μm. However, when it comes to the range of mid-IR as 8-12 μm, just a few materials can combine the desirable optical properties with favorable thermal stabilities and mechanical properties. ZnS is one of the limited optical ceramics that can be used for the 8-12 μm range due to its desirable transparency in the mid IR region and compromising thermal and mechanical properties. Thus, in the range of wavelength of 8-12 μm, ZnS ceramics can be a desirable candidate for the IR transparent ceramics used in military and commercial applications.

In 1950s, with increasing demands of the IR-transmitting materials, ZnS single crystals were grown in the Air Force labs and measured with various

properties.[49] Later, in the year of 1956, the researchers from Kodak applied hot pressing to consolidate ZnS powders into dense IR transparent ceramics, which led to the commercial productions of ZnS transparent ceramics.[50] From 1970's, polycrystalline ZnS transparent materials fabricated by CVD gradually replaced hot-pressed ZnS ceramics due to its capability of producing large pieces of high-purity ZnS with lower optical losses. Meanwhile, post HIP was then employed in the CVD ZnS materials to improve the transmittance in the range of visible light.[51]

However, the CVD process is expensive and time-consuming. In addition, the HIP process resulted in the sacrifice of mechanical strength and hardness due to the recrystallization and crystal growth during HIP.[52] Thus, researchers tried to synthesize ZnS particles using wet chemistry methods first and then consolidated the ceramics by hot pressing under a vacuum condition, which was a cost-effective method to fabricate dense ceramics at lower temperatures.[47] It has also been employed in various fabrications of different ceramics, such as transparent ceramics, electroceramics, and ultrahigh temperature ceramics.[15,53,54]

4. Photoluminescence of ZnS

As a favorable host, ZnS can be doped with various elements. The addition of dopants as activators into ZnS crystals, such as transition metals, rare earth elements, and halogen elements, can make ZnS-based materials produce photoluminescence characteristics. These ZnS-based materials are called ZnS-based phosphors.[55-62] Due to their prominent capability of being doped with various elements to bring out luminescence with a diversity of colors, ZnS-type phosphors are widely used in cathode ray tubes (CRT), radar screens, and lamps.[63,64]

Due to the quantum size confinement characteristic of materials in the nanometer scale leading to drastic difference from bulk materials, researchers have performed extensive studies on band gap increase and tunable photoluminescence emission of doped nanostructured ZnS.[65,66] Among the doped ZnS materials, Mn-doped ZnS has attracted extensive research interests because of its exceptionally

efficient light emitting properties. Tremendous studies have been conducted to investigate the structure, morphology, photoluminescence spectra characteristics, photoluminescence quantum efficiency and lifetime of the Mn-doped ZnS crystals.[67] It was reported that the Mn doped ZnS nanocrystals could lead to the emission of the orange light induced by the doping of Mn^{2+} as the luminescent center. Bedsides the Mn-doped ZnS with nanostructure, the nanostructured ZnS doped or codoped with various transition metals and rare earth elements, such as Cu, Ni, Co, Eu, Er, and Yb, are also of interest to researchers due to their distinctive photoluminescence properties.[65]

In addition, in recent years, it has been reported that undoped ZnS nanocrystals, nanotubes, nanobelts, nanoribbons and even as-sintered ceramics can exhibit green luminescence due to their various imperfections. Tsuruoka *et al.* investigated the green emission peak of ZnS nanobelts by applying scanning near-field optical microscopy and ascribed it to the line and planar defects, without further explanation on the specific defects.[68] Ye *et al*. revealed that the green photoluminescence band at 535 nm was related to elemental sulfur species on the surface of ZnS nanobelts.[69,70] According to the investigations by Chen *et al.*, the green luminescence was derived from the electronic states determined by zinc vacancies.[37,38] Nevertheless, Wang *et al.* claimed that the green luminescence was attributed to the electron transfer from sulfur vacancies to interstitial sulfur states. [71] For as-sintered undoped ZnS ceramics, J.C. Lee *et al.* reported the comparison of the luminescent properties of as-sintered ZnS sphalerite and wurtzite, and concluded that radiative transition from the level of sulfur vacancy to the valence band for charge compensation of Zn vacancy would lead to green emission in both pure sphalerite, and mixture of sphalerite and wurtzite.[72] Additionally, various intrinsic electronic defects within ZnS optical ceramics via CVD were studied to explain the photoluminescent properties for the ceramics.[73] However, very few studies were reported for the undoped ZnS ceramics sintered by FAST and VHP.

C. Aims of This Work

Through the research into the synthesis of ZnS powders via wet chemistry routes, consolidation of ZnS optical ceramics via FAST and VHP, and photoluminescence of ZnS optical ceramics, this present work aims to propose rational discussions on the processing, properties, and photoluminescence characteristics of ZnS optical ceramics to provide the reference for further and promising research on ZnS optical ceramics.

SYNTHESIS AND CHARACTERIZATION OF ZNS POWDERS

A. Introduction

As discussed earlier, in order to fabricate densified optical ceramics with desirable properties, to obtain raw powders with high purity and benign sintering properties is of critical significance. The microstructure and morphology of the starting powders are the determined factors for the quality of the sintered ceramics. Thus, to prepare consolidated ZnS ceramics with desirable optical properties, the foremost and threshold issue is to obtain desirable powders. For powder synthesis, compared with the conventional solid-state reaction method, wet chemistry precipitation has the advantages of synthesizing powders with finer particle size and easily controlled morphology. In this study, four different ZnS powders were synthesized by different wet chemical precipitation methods. In addition, ZnS powders from Sigma-Aldrich and jet milled ZnS single crystal flasks form Alfa were also characterized with the aim to compare microstructure, morphology and sintering properties between different ZnS powders.

B. Experimental Procedures

1. ZnS Powders Synthesis and Processing

Four ZnS powders were synthesized with different sources of sulfur and different pH values by colloidal processing.

- **ZnS powders synthesis with thioacetamide (TAA) as the sulfur source through a hot water bath under acidic conditions**

TAA was used as the sulfur source during the synthesis process of ZnS powders. A colloidal processing route including precipitation and hot water bath was performed to fabricate ZnS particles. Through hydrolysis and thermal decomposition under acidic conditions, TAA is capable of releasing H_2S for precipitation to serve as

sulfur source. HNO_3 was adopted to create an acidic solution environment for promoting the decomposition of TAA at high temperatures. The flowchart of the synthesis process is concisely displayed in Figure 1. First, thioacetamide (TAA, CH_3CSNH_2, ≥99.0%, Sigma Aldrich) and zinc nitrate hexahydrate ($Zn(NO_3)_2 \cdot 6H_2O$, ≥99.0%, Sigma Aldrich) with the stoichiometric ratio were completely dissolved in deionized water (DI water, Millipore Automatic Sanitization Module), respectively. Then the two solutions were mixed together by stirring and nitric acid (HNO_3, 70%, Sigma Aldrich) was added to the mixed solution to adjust pH to be acidic. Second, the solution was heated to 60 ºC-70 ºC in a hot water bath to encourage ZnS nanoparticles growth. As the reaction went on, the solution turned cloudy, indicating the agglomeration of crystallized ZnS particles. The suspension of ZnS colloids was then cooled to 0 ºC in an ice water bath to halt particle growth. The powders were then washed and centrifuged in both DI water and ethanol (Reagent alcohol, 100%, Decon), respectively (Allegra X-12 Centrifuge, Beckman Coulter). The precipitated ZnS powders were then dried in air.

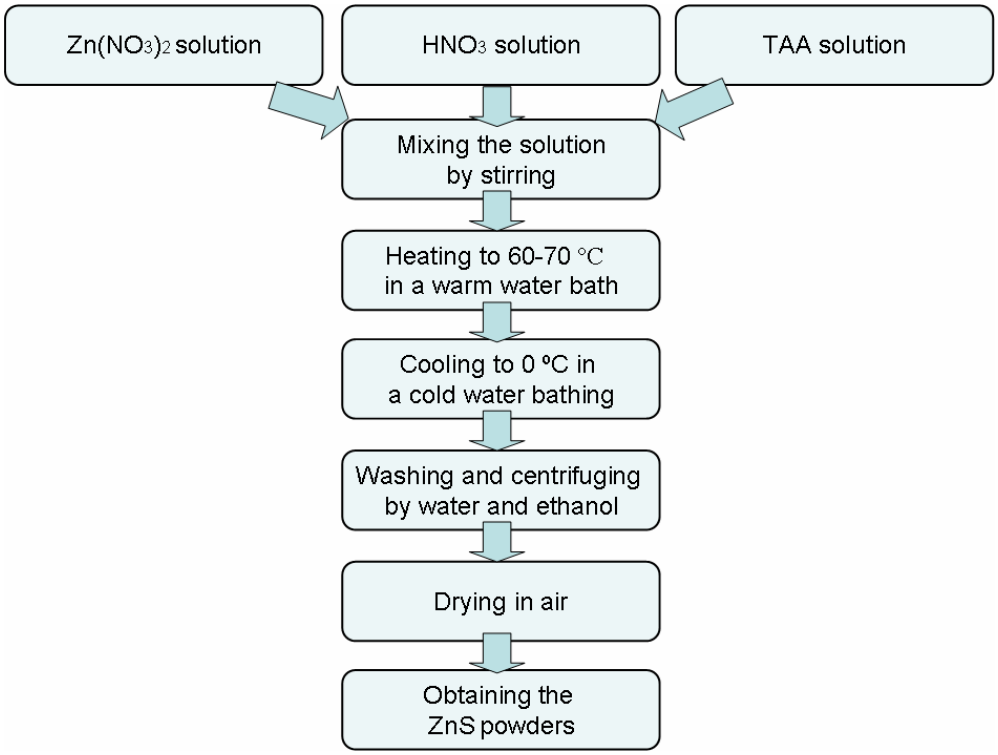

Figure 5. Flowchart of ZnS powders synthesis with TAA as the sulfur source via a hot water bath under acidic conditions.

- **ZnS powders synthesis with Na_2S as the sulfur source**

Na_2S was used as the sulfur source during the synthesis process of ZnS powders. A colloidal processing route for fast precipitation was performed to fabricate ZnS particles. Na_2S is capable of releasing S^{2-} in solution for the precipitation of S^{2-} and Zn^{2+} to ZnS. The flowchart of the synthesis process is concisely displayed in Figure 2. In the first step, $Zn(NO_3)_2 \cdot 6H_2O$ (≥99.0%, Sigma Aldrich) and sodium sulfide nonahydrate ($Na_2S \cdot 9H_2O$, ACS reagent, ≥98.0%, Sigma Aldrich) with the stoichiometric ratio were dissolved into DI water (Millipore Automatic Sanitization Module), respectively. HNO_3 (70%, Sigma Aldrich) was then added into $Zn(NO_3)_2$ solution to adjust the pH value to be acidic. Na_2S solution was then slowly added dropwise into $Zn(NO_3)_2$ solution while being stirred. As the two solutions were mixed together, the solution turned to a milky suspension with white color, indicating the production of ZnS particles. Finally, the colloids were collected, and then washed and centrifuged in both DI water and ethanol (Reagent alcohol, 100%, Decon), respectively (Allegra X-12 Centrifuge, Beckman Coulter). The precipitated ZnS powders were then dried in air.

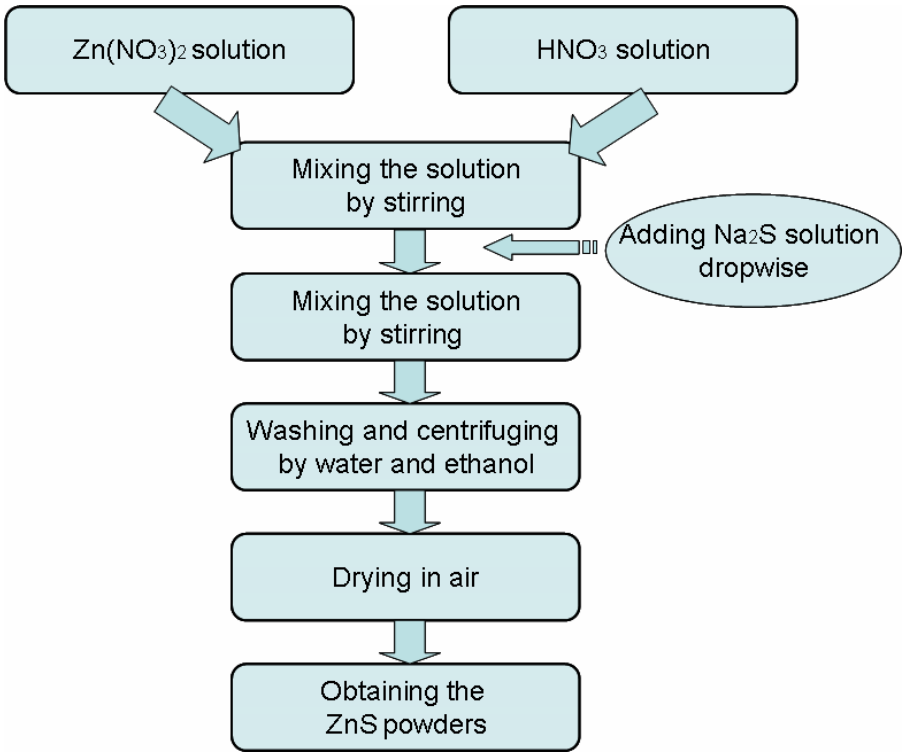

Figure 6. Flowchart of ZnS powders synthesis with Na_2S as the sulfur source.

- **ZnS powders synthesis with TAA as the sulfur source under basic condition**

TAA was used as the sulfur source during the synthesis process of ZnS powders. A colloidal processing route for fast precipitation was performed to fabricate ZnS particles. The flowchart of the synthesis process is concisely displayed in Figure 7. Firstly, TAA (≥99.0%, Sigma Aldrich) and $Zn(NO_3)_2 \cdot 6H_2O$ (≥99.0%, Sigma Aldrich) with the stoichiometric ratio were dissolved in DI water (Millipore Automatic Sanitization Module), respectively. Then the two solutions were mixed together and ammonium hydroxide solution (NH_4OH, 28.0%-30.0%, Sigma Aldrich) was added into the mixed solution to adjust the pH to be basic. The solution turned cloudy indicating the formation of ZnS particles. Finally, the ZnS colloids were collected, and then washed by water and ethanol (Reagent alcohol, 100%, Decon), respectively (Allegra X-12 Centrifuge, Beckman Coulter, USA). The ZnS suspension was put into an oven to be dried in air to obtain ZnS powders.

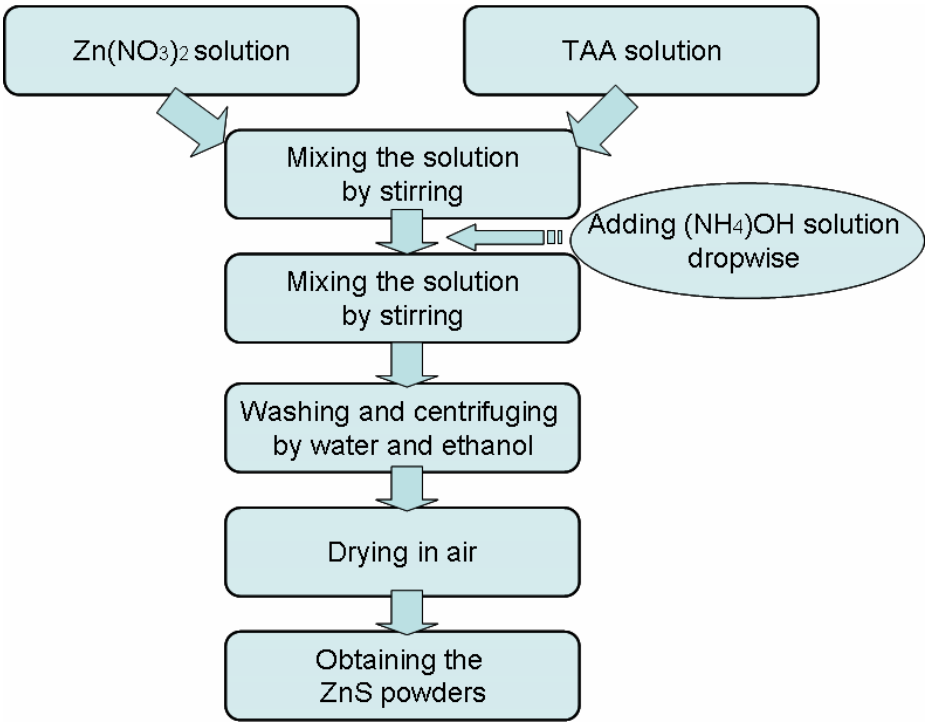

Figure 7. Flowchart of ZnS powders synthesis with TAA as the sulfur source under basic conditions.

- **ZnS powders synthesis with $(NH_4)_2S$ as the sulfur source**

$(NH_4)_2S$ was used as the sulfur source during the synthesis process of ZnS powders. A colloidal processing route for fast precipitation was performed to fabricate ZnS particles. Similar to Na_2S, $(NH_4)_2S$ is capable of releasing S^{2-} in solution for the precipitation of S^{2-} and Zn^{2+} to ZnS. The flowchart of the synthesis process is concisely displayed in Figure 8. In the first step, $Zn(NO_3)_2 \cdot 6H_2O$ (≥99.0%, Sigma Aldrich) and ammonium sulfide ($(NH_4)_2S$, 20 wt. % in H_2O, Aldrich) solution with the stoichiometric ratio were dissolved into DI water (Millipore Automatic Sanitization Module), respectively. HNO_3 (70%, Sigma Aldrich) was then added into the $Zn(NO_3)_2$ solution to adjust the pH value to be acidic. Next, the $(NH_4)_2S$ solution was slowly added drop-wise slowly into the solution of salts. The mixing of the two solutions resulted in immediate clouding within the solution with yellowish white precipitates forming, indicating the formation of ZnS particles. Finally, the ZnS colloids were collected, and then washed and centrifuged in both DI water and ethanol (Reagent alcohol, 100%, Decon), respectively (Allegra X-12 Centrifuge, Beckman Coulter). The ZnS suspension was put into an oven to be dried in air to obtain ZnS powders.

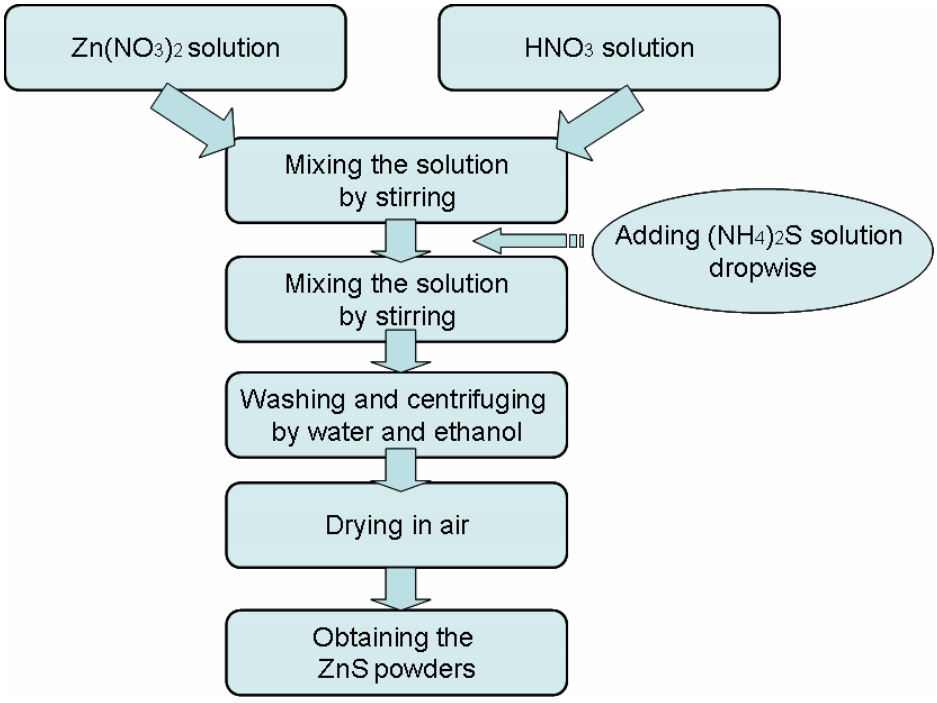

Figure 8. Flowchart of ZnS powders synthesis with $(NH_4)_2S$ as the sulfur source.

To make a comparison with the synthesized powders, the ZnS powders from Sigma-Aldrich were used as received and the ZnS single crystal flakes from Alfa were jet milled into finer powders.

2. Characterization of ZnS Powders.

All the studied ZnS powders were measured via X-ray diffraction (XRD, D2 PHASER, Bruker) equipped with a CuKα radiation (30 kV, 10 mA) to characterize initial phase composition, with the measurement conditions of 10 to 75 º2θ, step size 0.02 º2θ and 0.3 second count time. The MDI Jade 9 was adopted for phase analysis. Pesudo-Voigt method was used to fit the peaks in XRD patterns of the studied ZnS powders by Topas (Bruker) to carry out the crystallite size calculation. The morphological and structural features of the ZnS powders were investigated by environmental scanning electron microscopy (SEM, Quanta 200, FEI). Secondary electron (SE) and backscattered electron (BSE) images were both taken. Tristar II 3020 system (Micromeritics) was employed to detect the surface area and adsorption-desorption curve of the synthesized ZnS powders using Barret-Joyner-Halenda (BJH) and Brunauer–Emmett–Teller (BET) methods. The powders were degassed at 25 ºC for 10 min and at 150 ºC for 1 hour before the measurement.

C. Results and Discussion

Figure 9 shows the XRD patterns of the as-synthesized and commercial ZnS powders. All the synthesized ZnS powders are indexed to have the pure cubic sphalerite phase (ICDD card no. 04-001-6857, F-43m, a = b = c = 5.40 Å). However, for the commercial ZnS specimens, several additional peaks are shown in the patterns besides the cubic ZnS phase, which are indexed to hexagonal wurtzite (ICDD card no. 04-008-7254, $P6_3mc$, a = b = 3.82 Å, c = 6.26 Å). In addition, more peaks of wurtzite are shown in the XRD pattern of the jet milled ZnS powders, suggesting a lager amount of wurtzite within the sample. It should be noted that the peak widths shown

in the XRD pattern form different ZnS powders show apparent difference, due to different crystallite sizes of the powders. The crystallite size is inversely proportional to the FWHM of the peaks, according to Debye-Scherrer equation:

$$L = \frac{0.9\lambda}{\mathrm{B}\cos\theta} \quad (1)$$

where L is the crystallite size, λ is the wavelength of the X-ray radiation, B is the FWHM (full width at half maximum) in units of radians, and θ is the Bragg angle of the peak.[74] It is indicated that the ZnS powders synthesized by wet chemistry methods have smaller crystallite size with broaden peak width than the commercial powders. Detailed observation reveals that crystallite size of the different synthesized ZnS powders based on the difference of the sulfur sources and synthesis methods.

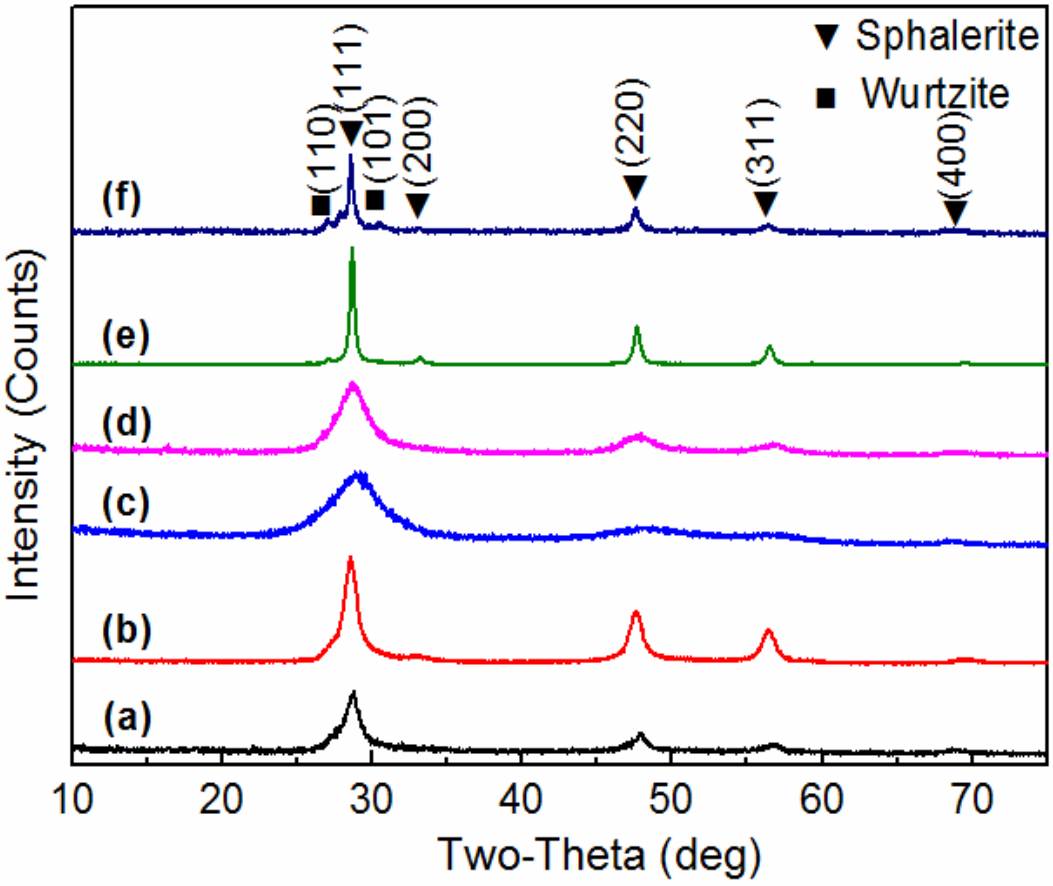

Figure 9. XRD patterns of different ZnS powders (a: with TAA and hot water bath; b: with Na_2S; c: with TAA under basic condition; d: with $(NH_4)_2S$; e: from Sigma-Aldrich; f: jet milled single crystal flakes from Alfa).

The SEM images showing the morphology and microstructure of the studied ZnS powders are displayed in Figure 10. It is shown that the commercial ZnS powders have larger particle size in micron scale. The ZnS powders from Sigma have apparent agglomerations of about 5-8 ± 1 μm. High-energy Jet milling can be beneficial to break the single crystal flakes into particles of about 1 ± 0.5 μm. Compared with the commercial powders, the synthesized powders have small particle size at submicron scale or nanoscale, which is attributed to the solution-based wet chemistry synthetic methods that control the particle growth. Different from the other three synthesized ZnS powders with obvious inhomogeneous aggregations of nanoparticles, ZnS powder synthesized through hot water bath route has homogeneous spherical submicron particles. It is the hot water route that enables the homogeneous particle growth. ZnS nanoparticles first nucleate, and then gradually grow to larger particles at elevated temperatures via hot water bath, resulting in slow and homogenous precipitation.

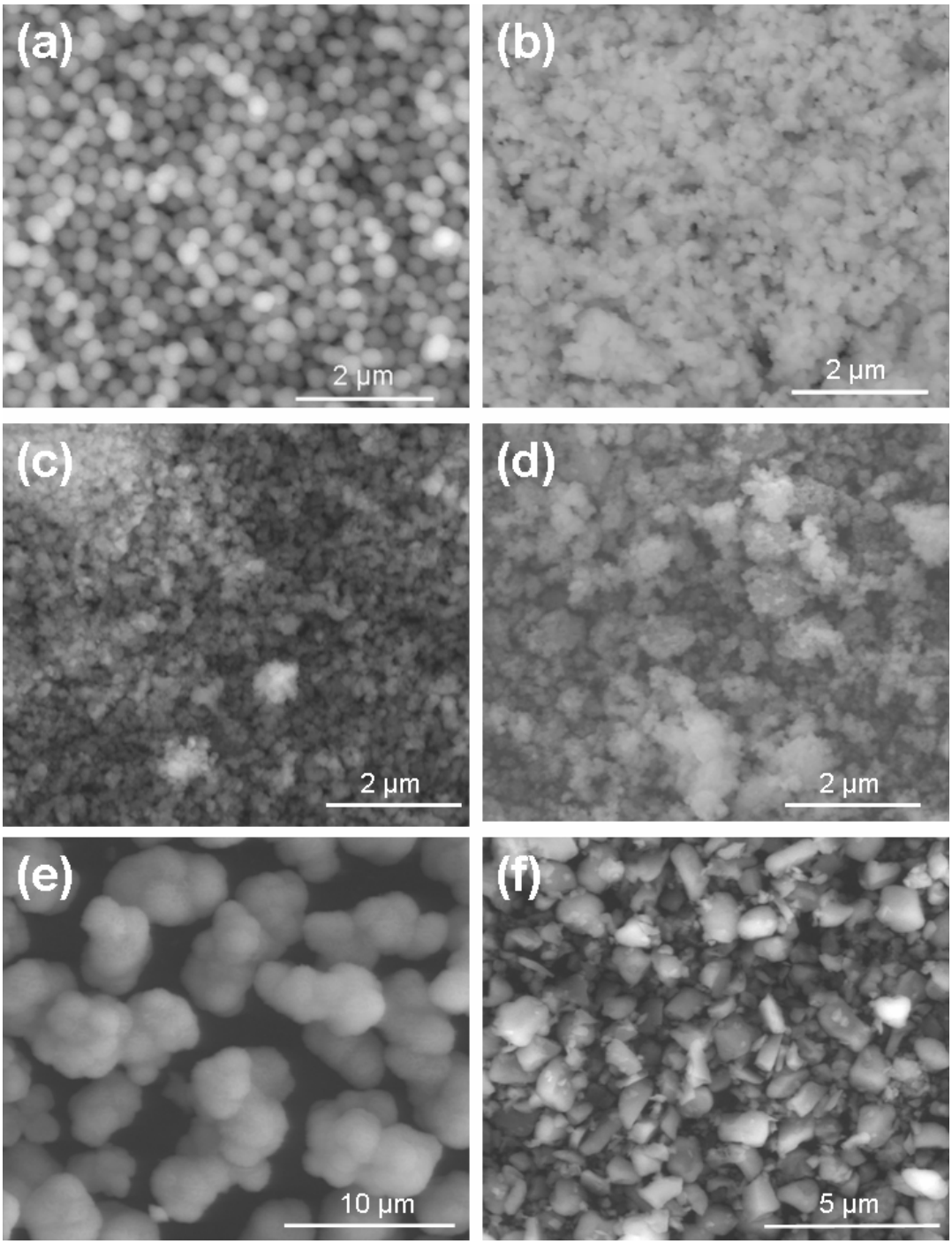

Figure 10. SEM images of different ZnS powders (a: with TAA and hot water bath; b: with Na_2S; c: with TAA under basic condition; d: with $(NH_4)_2S$; e: from Sigma-Aldrich; f: jet milled single crystal flakes from Alfa).

The studied ZnS powders were further characterized by the BET method to measure the surface area. Table II shows the specific surface areas of the ZnS powders.

The result is in accordance with the XRD and SEM results. The powders with smaller particle size and crystallite size tend to have a corresponding increase in specific surface area. The synthesized ZnS powders have much larger surface area than the commercial powders, indicating larger surface energy of the synthesized powders. It is assumed that different specific surface areas of the synthesized ZnS powders are correlated to different synthetic routes with different sulfur sources. In addition, it should be noted that higher specific areas correspond to higher estimated standard deviations, which may be due to the larger number of pores. Further investigation is needed to confirm the reason.

It is also demonstrated that agglomerations occur within the synthesized ZnS particles. If the particle was spherical and non-porous, the average particle size could be calculated based on the equation:

$$SSA=6/\rho_s D \tag{2}$$

where *SSA* refers to the specific surface area, ρ_s corresponds to the density of the samples, and *D* is the mean diameter of the particles. For example, according to the specific surface area value of 75.38 m^2/g, and sphalerite density of 4.10 g/cm^3, the mean diameter of the particles within ZnS powder synthesized by using TAA and hot water bath is calculated to be 19.41 nm. However, the displayed average particle size in SEM images is around 200 nm, which is much larger than the calculated one. Therefore, it is considered that the particles shown in the SEM image are actually porous. In addition, for the other synthesized powders, the calculated mean particle size can not match the average particle size observed from the SEM figures. Thus, it is concluded that the large particles shown in the SEM images for the synthesized powders are actually porous agglomerations of small ZnS particles or crystallites.

Table II. BET Specific Surface Area for the Studied ZnS Powders

ZnS powder	Specific surface area (m^2/g)	Estimated standard deviation (m^2/g)
TAA & hot water bath	75.38	0.35
Na_2S	101.43	0.40
TAA & basic condition	189.20	0.56
$(NH_4)_2S$	229.70	2.43
Sigma-Aldrich	19.81	0.06
Alfa & jet milled	5.30	0.04

Figure 11 and Figure 13 show the adsorption-desorption curves of the synthesized ZnS powders and commercial ZnS powders, respectively. As can be seen from the figures, all the synthesized ZnS powders have the type IV isotherm curves, and the hysteresis indicates that some mesopores exist in the powders. The commercial powders from Sigma also have the IV isotherm curves with hysteresis, suggesting the presence of mesopores. However, the jet milled ZnS single crystal flakes have the type III isotherm curve with no hysteresis. It is considered that the jet milling is only capable of reducing the particle size for the single crystal flakes. This can also explain the low specific surface are of the sample. The detailed pore size distribution curves of the synthesized and commercial ZnS powders are exhibited in Figure 12 and Figure 14. Presence of the mesopores within the synthesized powders and commercial powders from Sigma is confirmed from the curves. Additionally, some macropores larger than 50 nm can also be detected. It is noteworthy that the powders synthesized through hot water bath have narrow pore distribution in the 2-5 nm range. The presence of the mesopores and macropores can lead to the high specific surface area of the ZnS powders.

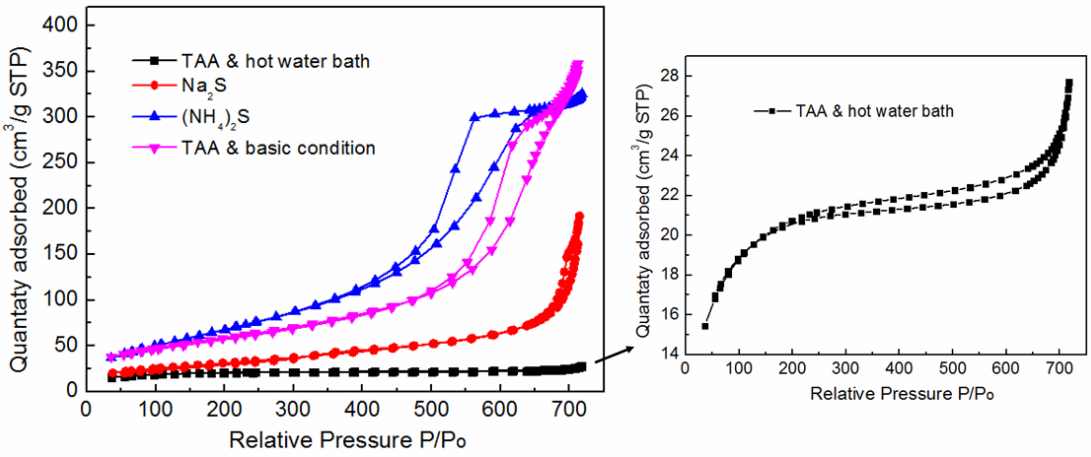

Figure 11. Adsorption-desorption curves of the synthesized ZnS powders.

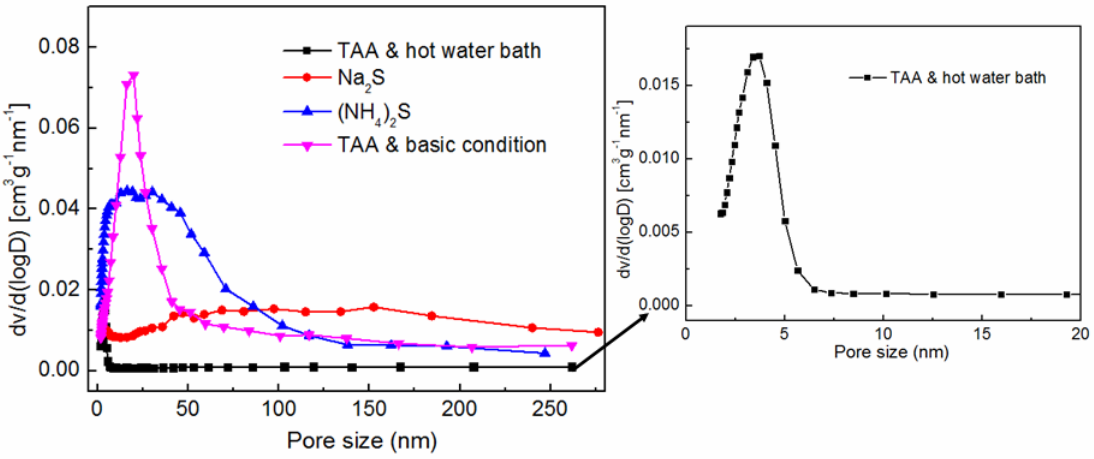

Figure 12. Pore size distribution curves of the synthesized ZnS powders.

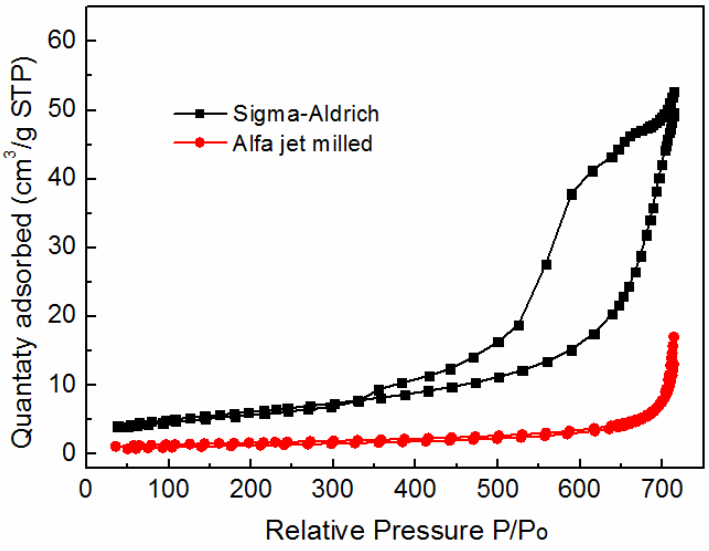

Figure 13. Adsorption-desorption curves of the commercial ZnS powders.

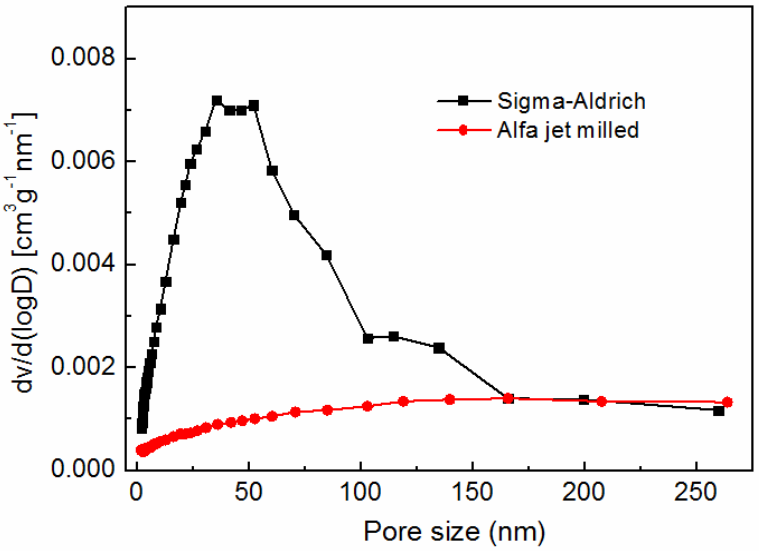

Figure 14. Pore size distribution curves of the commercial ZnS powders.

The difference in microstructure and morphology of the synthesized ZnS powders is ascribed to the synthesis methods and sulfur sources. The ZnS particles are formed by the precipitation of Zn^{2+} and S^{2-}. For the ZnS powders prepared by using TAA as the sulfur source with hot water bath, the reaction proceeds as follows:

$$CH_3CSNH_2 + H_2O \xrightarrow{H^+} CH_3CONH_2 + H_2S \quad (3)$$

$$HS^- \longrightarrow H^+ + S^{2-} \quad (4)$$

$$Zn^{2+} + S^{2-} \longrightarrow ZnS \quad (5)$$

For the ZnS powders synthesized by using Na_2S as the sulfur source, the synthesis reaction proceeds as below:

$$Na_2S \longrightarrow 2Na^+ + S^{2-} \quad (6)$$

$$Zn^{2+} + S^{2-} \longrightarrow ZnS \quad (7)$$

For the ZnS powders synthesized by using $(NH_4)_2S$ as the sulfur source, the synthesis reaction procedures are shown as follows:

$$(NH_4)_2S \longrightarrow 2NH_4^+ + S^{2-} \quad (8)$$

$$Zn^{2+} + S^{2-} \longrightarrow ZnS \quad (9)$$

For the ZnS powders synthesized by using TAA as the sulfur source under basic condition, the reaction proceeds as below:

$$CH_3CSNH_2 + 2NH_4(OH) \longrightarrow CH_3C(NH_2)NH + NH_4^+ + HS^- + 2H_2O \quad (10)$$

$$HS^- \longrightarrow H^+ + S^{2-} \quad (11)$$

$$Zn^{2+} + S^{2-} \longrightarrow ZnS \quad (12)$$

As can be seen from the SEM images, the ZnS powders synthesized by using TAA as the sulfur source through hot water bath have homogeneous spherical particles. Figure 15 shows the growth schematics of the synthesized ZnS powders with hot water bath route and at room temperature, respectively. It is known that the formation processes of the particles through wet chemistry synthesis include two stages, nucleation and growth.[75] For the ZnS powders synthesized through the colloidal processing under acidic conditions and via a hot water bath route, ZnS nanoparticles first nucleate in the mixed solution, and then gradually grow to submicron particles at elevated temperatures, resulting in slow and homogenous precipitation. The ZnS agglomeration particle size can be controlled through adjusting the reaction time at elevated temperatures. However, nucleation and growth take place simultaneously for the other three synthesized ZnS powders, making it difficult to control the particle size, leading to inhomogeneous growth and agglomeration of ZnS particles. In addition, due to the temperature difference of ZnS particle syntheses, the synthesized ZnS powders via colloidal processing with hot water bath has less pores with narrower size distribution because of the homogeneous particle growth at higher temperatures, contributing to the lower surface area of the powders compared with the ZnS powders synthesized at room temperature, which is shown in the specific surface area data.

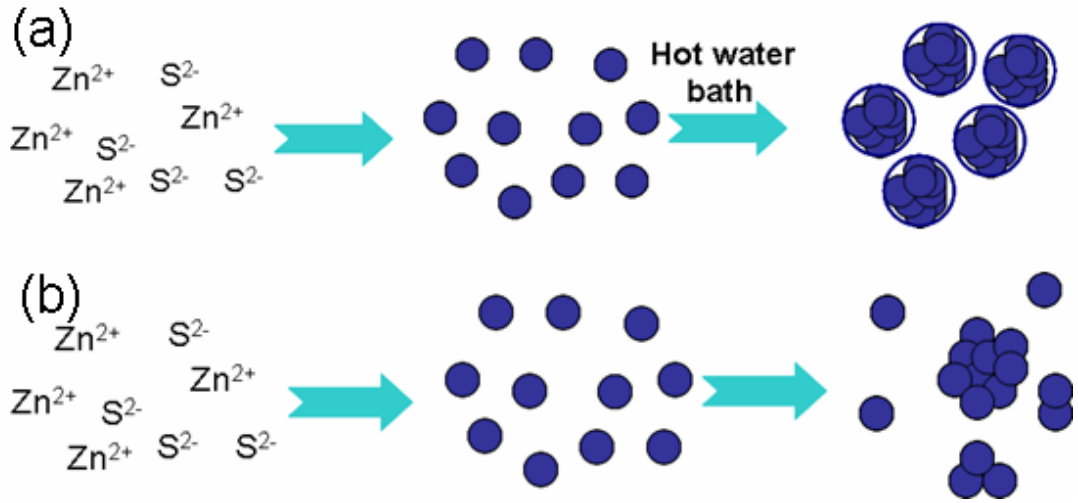

Figure 15. Growth schematics of the ZnS powders synthesized through the colloidal processing with hot water bath route (a) and at room temperature (b).

D. Conclusions

In summary, this chapter discusses the characterization of four ZnS powders synthesized through wet chemistry methods and two commercial ZnS powders. All the synthesized ZnS powders have pure cubic ZnS sphalerite phase, while both commercial ZnS samples have the minor phase as hexagonal wurtzite. With small crystallites and particles, the synthesized ZnS powders are porous and have large specific surface area. In addition, the ZnS powders synthesized using TAA as the sulfur source through a hot water bath under acidic conditions the have homogeneous spherical particles, due to the homogenous precipitation of ZnS particles.

CONSOLIDATION OF ZNS OPTICAL CERAMICS

A. Introduction

To avoid or eliminate the scattering loss is vital to attaining desirable transparency for optical ceramics. Consolidation of ceramics plays an important role in removing pores and obtaining high densification, making it a critical step during the processing of optical ceramics with excellent optical properties. In addition, the consolidation of ZnS ceramics is also a direct way to prove and confirm the sintering properties of the raw powders. In this chapter, two pressure-assisted sintering techniques were employed for consolidation of the studied ZnS powders. First, four synthesized ZnS powders and two commercial ZnS powders were consolidated by field assisted sintering technique (FAST) in order to investigate the sintering properties of the raw powders. The powders with beneficial sintering properties determined by FAST were selected to be sintered by vacuum hot pressing (VHP) to fabricate ZnS optical ceramics. The as-sintered ZnS ceramics were characterized with phase composition, microstructure and optical properties. Studies on consolidation behavior of the different powders are also performed in order to correlate the processing methods of ZnS powders and ceramics to optical properties of the ZnS ceramics. The grain growth and densification mechanism for VHP was briefly discussed.

B. Experimental Procedures

In order to obtain ZnS ceramics, the four heat-treated synthesized powders with two commercial ZnS powders were sintered using FAST. Figure 16 shows the schematic of the FAST unit configuration construction. It is a pressure-assisted sintering approach that employs the pulsed direct current to generate Joule heat on graphite punches to heat powder compacts, which enables fast sintering at reduced temperature. Here, as the advantages of FAST, high heating rate and short dwell time were applied in the experiments. The heat-treated ZnS powders were loaded into a

graphite die with a diameter of 18.75 mm, and graphite foils (thickness of 0.5 mm) were used to separate the sample from punches. The powders were consolidated at the range of 750-850 ºC for 20-60 min under a uniaxial pressure of 30-100 MPa at a heating rate of 50-100 ºC /min in a low-level vacuum condition by FAST (HP D 25, FCT Systeme GmbH). An optical pyrometer was used to monitor the temperature.

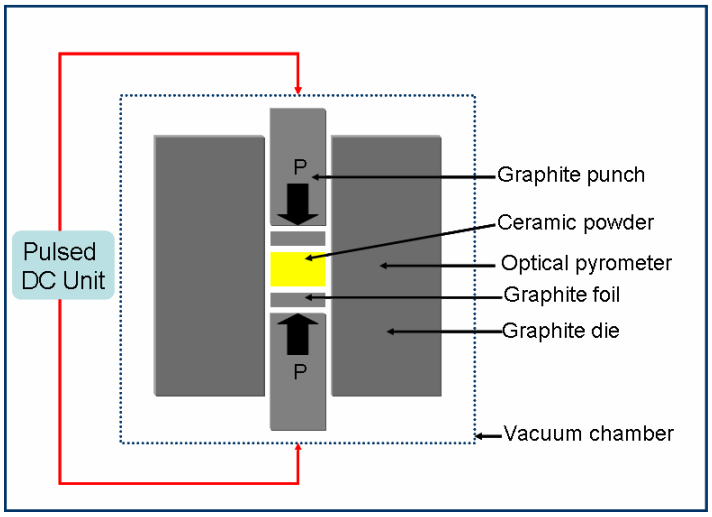

Figure 16. Schematic view of the FAST furnace configuration.

According to the results of the ZnS ceramics sintered by using different raw powders, two ZnS powders that contribute to better optical properties of the ZnS ceramics sintered by FAST were selected to be sintered by VHP, to make a comparison between the two sintering techniques. Figure 17 exhibits the schematic of the VHP unit configuration. Added with a vacuum condition in addition to hot pressing, VHP is more advantageous for densification and for the avoidance of the oxidation of ZnS. The ZnS powders were loaded into a graphite die with a diameter of 18.75 mm (another graphite die with a diameter of 10.00 mm) and graphite foils (thickness of 0.50 mm) were used to separate the sample from punches. The powders were consolidated at 900-1000 ºC for 1-4 hours under a uniaxial pressure of 30-100 MPa at a heating rate of 2-10 ºC/min in a high-level vacuum condition by VHP (OTF-1200X-VHP4, MTI).

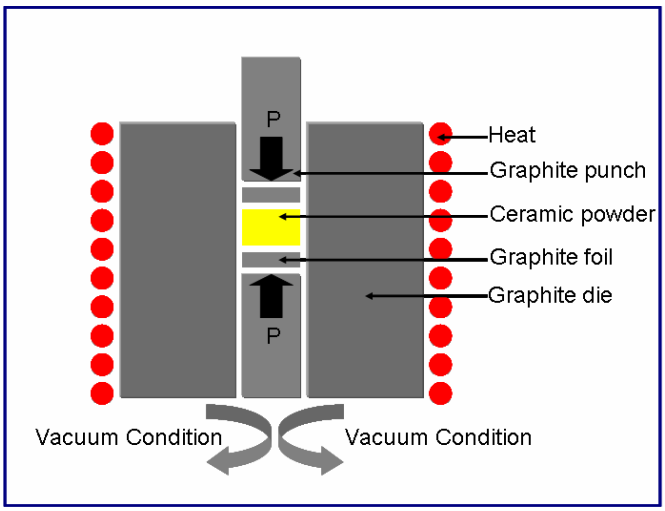

Figure 17. Schematic view of the VHP furnace configuration.

Phase composition of the ZnS sintered ceramics was determined using XRD with CuKα (λ= 0.154 nm) radiation (D2 PHASER, Bruker). MDI Jade 9 was adopted for phase analysis, and the Pseudo-Voigt method was used to fit the XRD pattern for the sintered ceramics employing Topas analysis software (Bruker) to calculate the phase composition. The morphological and structural features of the ZnS powders and as-sintered ceramics were investigated by scanning electron microscopy (SEM, Quanta 200, FEI). Archimedes's method was adopted to measure the density of the as-sintered ZnS ceramics. Fourier transform IR spectroscopy (FTIR, Nicolet 6700, Thermo Fisher) was applied to measure the transmittance of the polished ceramic pellets.

C. Results and Discussion

1. ZnS Ceramics Consolidated via FAST.

The XRD patterns of the all ZnS ceramics sintered at 850 ºC are shown in Figure 18. As can be seen from the figure, cubic sphalerite (ICDD card no. 04-001-6857, F-43m, a = b = c = 5.40 Å) and hexagonal wurtzite (ICDD card no. 04-008-7254, $P6_3mc$, a = b = 3.82 Å, c = 6.26 Å) coexist within the ZnS samples, except for the sample using the powders with Na_2S as the sulfur source. The results

suggest a phase transition occurring earlier in the sintering process, at lower temperature than the transition temperature (1020 ºC) for ZnS bulks, which is attributed to the much smaller particle size of the ZnS powder as compared with that of the bulk ZnS. It has been reported by multiple authors that the activation energy for the sphalerite to wurtzite phase transition is dependent on particle size.[76-78] The kinetic mechanism by which the phase transition occurs during the sintering of powders with small particle size is likely different from that for ZnS bulks. In addition, the surface Gibbs free energy difference, which contributes to the energetic favorability of a phase transition, is also dependent on particle size.[43,79] Thus, the higher enhanced surface energy of micron-scale and nano-scale ZnS powder facilitates the phase transition at lower temperature. For the commercial ZnS samples, similar to the raw powders, the as-sintered ceramics also have the mixture of the two phases, but the relative intensity of the peaks corresponding to wurtzite is higher, due to the presence of ZnS wurtzite within raw ZnS powders, and phase transformation from cubic ZnS sphalerite to hexagonal ZnS wurtzite.

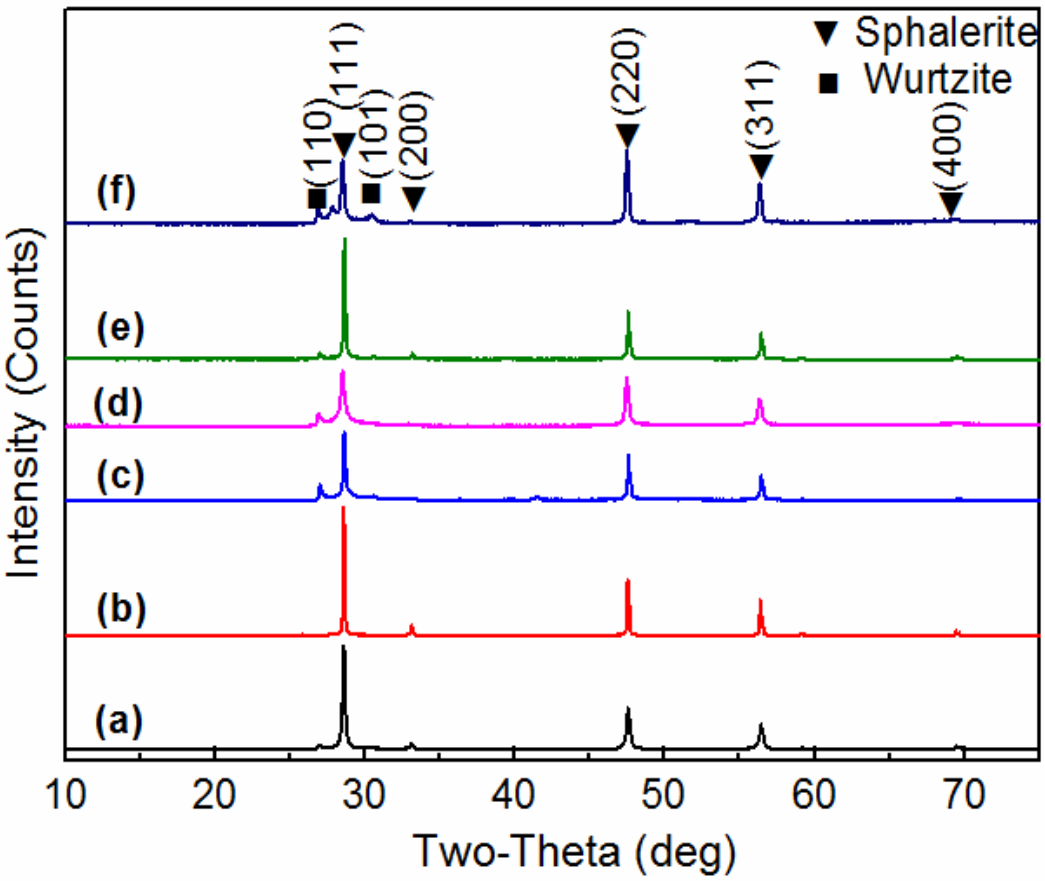

Figure 18. XRD patterns of ZnS ceramics sintered via FAST by using different ZnS powders (a: TAA with hot water bath; b: Na_2S; c: TAA under basic condition; d: $(NH_4)_2S$; e: Sigma; f: jet milled single crystal flakes from Alfa).

Figure 19 displays the corresponding SEM images of the fracture surfaces of the as-sintered ZnS ceramics. It is shown that all the samples have dense microstructures with a little residual porosity, indicating that FAST is an effective sintering technique to fabricate densified ZnS ceramics. Compared with the raw powders, the grains within ceramics are larger than the particles in powders shown in SEM images. It is easily explained by the grain growth during sintering including both the heating up process and dwelling process. This is also in accordance with the sharper and narrower peaks in XRD patterns indicating the growth of the crystallites. In addition, it should be noted that the ZnS raw powders with smaller particles and higher specific surface area have corresponding smaller grains.

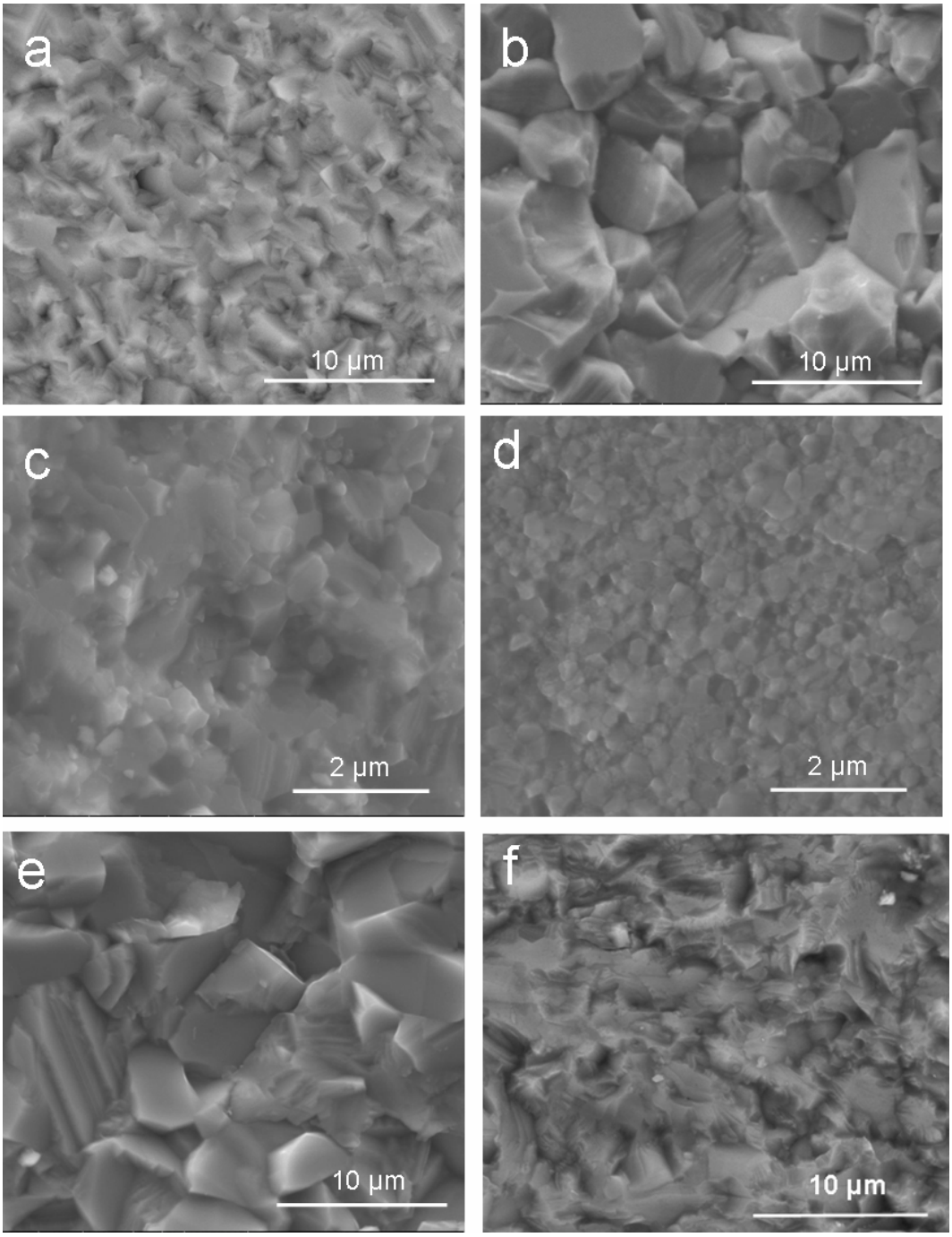

Figure 19. SEM images of ZnS ceramics sintered via FAST by using different ZnS powders (a: TAA with hot water bath; b: Na_2S; c: TAA under basic condition; d: $(NH_4)_2S$; e: Sigma; f: jet milled single crystal flakes from Alfa).

To directly evaluate optical properties of the samples, FTIR was adopted to measure the IR transmittance. Figure 20 exhibits the IR transmittance curves of the as-sintered ZnS ceramics. It can be seen that only two samples have desirable optical

transmittance in the mid-IR range. One is the sample sintered by using the powders synthesized with TAA via a hot water bath, and the other is the sample consolidated by the jet milled ZnS single crystals flasks from Alfa. The maximum optical transmittance reaches 61.3% at 11.8 μm. As discussed earlier, besides the high purity of the raw powders, high densification is also essential to the optical properties. The synthesized powders with small particle size and high surface free energy can contribute to densification. However, based on the optical properties results, since the raw powders for the samples with good optical properties both have homogenous particles, it is considered that the small homogeneous and monodisperse ZnS particles should be more favorable to ceramics consolidation. In addition, as shown in the relative density results in Table III, the two samples with better optical properties also have higher relative densities than others.

It should be noted that the samples have some absorption bands in the FTIR spectra. The peaks in the spectra at 15.0-25.0 μm correspond to the Zn-S characteristic vibrations. The bands at 2.5-5.0 μm are due to the Zn-S microstructure formations. The peaks at 5.0-13.5 μm are attributed to the C-C or C=C bands arising from graphite penetration into the sintered ceramics. It needs to be emphasized that the grey color shown on the samples from the photo images indicates the presence of carbon contamination. Under the effect of electric field, the diffusion of carbon from graphite to samples will be initiated and promoted due the highly conductive nature of graphite, resulting in the dark color of the samples and deterioration of optical property. Due to the double refraction and the difference in refractive index between cubic sphalerite and hexagonal wurtzite, the presence of hexagonal ZnS wurtzite can also affect the optical performance. Additionally, it is noticed that the two samples sintered by using the ZnS powders with higher specific surface area tend to have different spectra, and the optical transmittance is very low. Bearing in mind that these two powders are high-porosity, we assume that the difference in spectra because of undetected ZnO impurity, which is generated from reaction of ZnS with the residual oxygen in pores. The impurity phase will be harmful to optical transmittance due to

the difference of the refractive index for ZnO (2.0034) and ZnS (sphalerite: 2.3677).

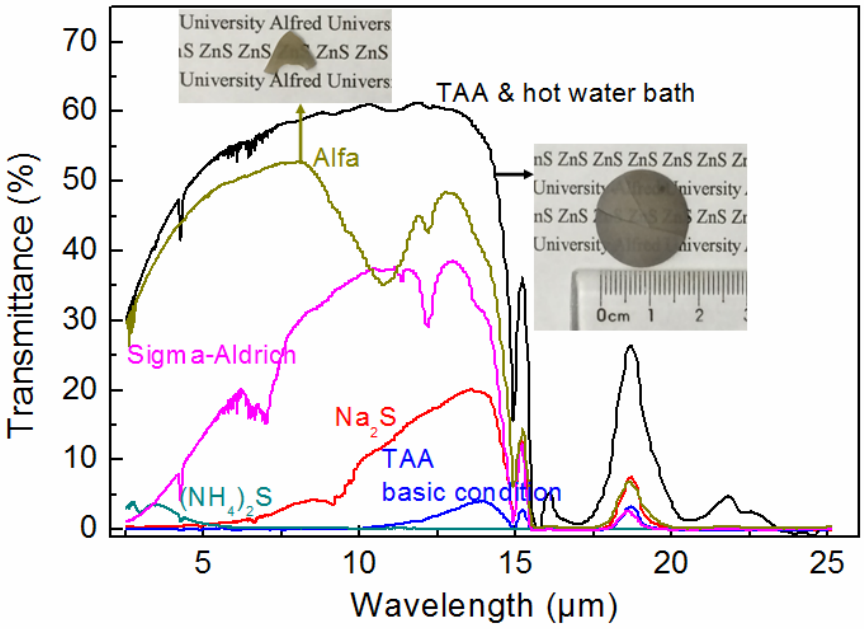

Figure 20. IR transmittance curves of the as-sintered ZnS ceramics consolidated by using different ZnS powders via FAST and photo images of the two ZnS ceramic samples with better optical properties (inset).

Table III. Relative Densities of the ZnS Ceramics Sintered by FAST

ZnS sample	Relative density (%)	Estimated standard deviation (%)
TAA & hot water bath	98.35	0.38
Na_2S	97.52	0.30
TAA & basic condition	98.05	0.31
$(NH_4)_2S$	97.78	0.46
Sigma-Aldrich	98.03	0.37
Alfa & jet milled	98.12	0.53

It should be noted that the sample sintered by using the synthesized ZnS powders have better optical performance by a comparison between the best two samples. This can also be demonstrated by the densification behavior. Figure 21

shows the actual temperature and piston speed dependence of time during the FAST process for the two ZnS powders contributing to better optical properties of the as-sintered ZnS ceramics. The maximum piston speed indicates the occurrence of maximum shrinkage and densification. It can be observed that the synthesized ZnS powders reach the maximum densification at a lower temperature than the commercial powders, indicating a faster densification rate of the particles with better sintering properties.

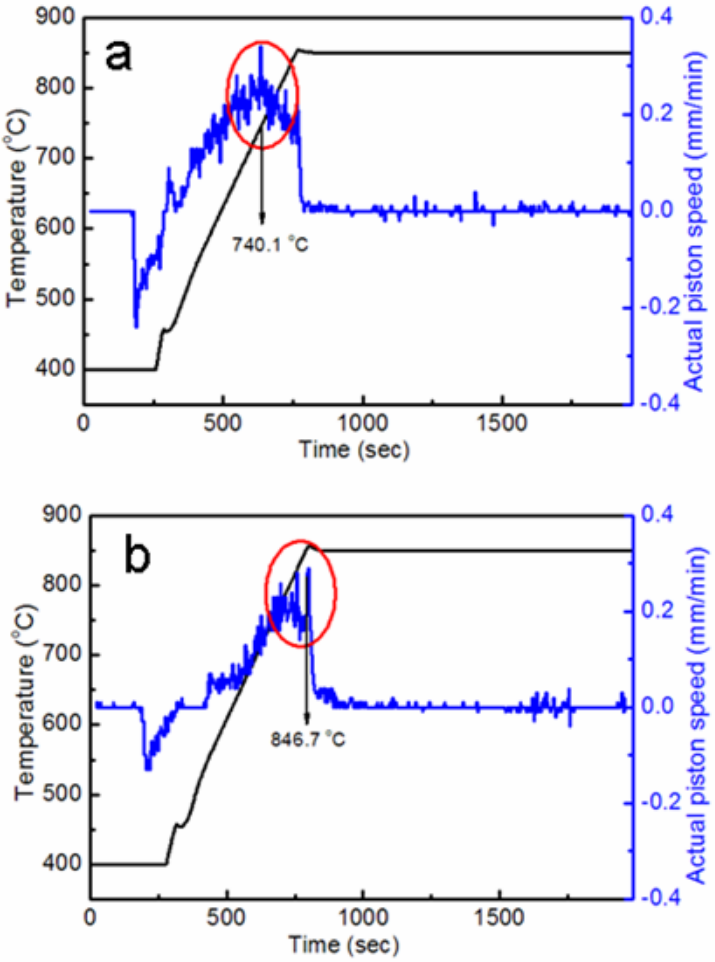

Figure 21. Actual temperature and piston speed dependence of time during the FAST process for the two ZnS powders (a: TAA & hot water bath; b: Alfa & jet milled).

2. ZnS Ceramics Sintered via VHP.

Based on the results of the ZnS ceramics sintered by using different raw powders, it is found that the ZnS powders synthesized by using TAA via a hot water

under acidic conditions and the jet milled ZnS single crystal flakes from Alfa can contribute to the samples with better optical performance. Thus, to make a comparison with FAST, the two ZnS powders were further sintered at 1000 ºC by VHP.

As shown in the XRD pattern in Figure 22(a), cubic sphalerite (ICDD card no. 04-001-6857, F-43m, a = b = c = 5.40 Å) and hexagonal wurtzite (ICDD card no. 04-008-7254, $P6_3mc$, a = b = 3.82 Å, c = 6.26 Å) coexist within the ZnS ceramics (TAA & hot water bath) sintered by VHP at 1000 ºC. It is reported that the phase transition temperature of bulk ZnS from sphalerite to wurtzite is 1020 ºC.[48] Here, it is considered that the small ZnS particles with higher surface energy will facilitate the phase transition, resulting in early phase transition lower than 1020 ºC.[80] Through fitting the XRD pattern by pseudo-Voigt method, the phase composition of the ceramics is determined to be 93.34 ± 0.35 wt% of sphalerite and 6.66 ± 0.35 wt% of wurtzite. The grains and microstructure of the sintered ZnS ceramics can be clearly observed from Figure 22(b). The grain size is from 1 μm to 4 μm and the ceramics are fully densified without low residual porosity. Compared with the sample sintered via FAST, it has larger grain size due to the slower heating rate and longer dwell time. The density for the ZnS ceramics is measured to be 4.092 ± 0.005 g/cm^3, 99.76 ± 0.12 % of the theoretical density (4.102 g/cm^3), which also confirms that ceramics are highly consolidated. The small difference between the two densities is attributed the existence of wurtzite phase with a smaller density (3.980 g/cm^3).

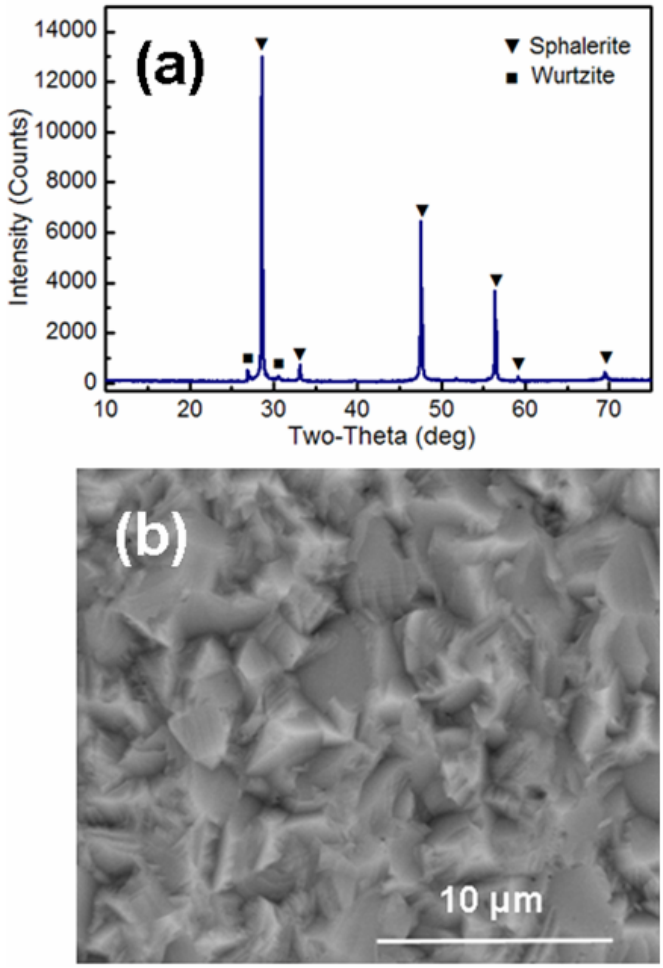

Figure 22. XRD pattern (a) and SEM micrograph (b) of the fracture surface for the as-sintered ZnS ceramics (TAA & hot water bath) by VHP.

Figure 23 shows the XRD pattern (a) and SEM image (b) of the as-sintered ZnS ceramics (Alfa & jet milled) by VHP at 1000 ºC. It can be observed that the sample also has the main phase as cubic sphalerite (83.79 ± 0.61 wt%) and the minor phase as hexagonal wurtzite (16.21 ± 0.61 wt%). In addition, the polytype of 4H-wurtzite phase is also present within the sample, besides the 2H-wurtzite phase. It is indicated that the earlier phase transformation also occurs based on the comparison of XRD patterns between raw powders and as-sintered ceramics. As can be seen in the SEM image, the ceramics with micron-sized grains are also fully consolidated. The density for the ZnS ceramics is measured to be 4.084 ± 0.012 g/cm^3, 99.55 ± 0.27% of the theoretical density (4.102 g/cm^3), confirming the high densification of

the ZnS ceramics. It is indicated that the density of the sample sintered using commercial ZnS powders is a bit lower than the other, which can be ascribed to larger amounts of wurtzite existing within the as-sintered ZnS ceramics (Alfa & jet milled). The presence of ZnS wurtzite results in the deterioration of the optical properties of the ZnS ceramics, due to the double refraction and the difference in refractive index between cubic sphalerite and hexagonal wurtzite.

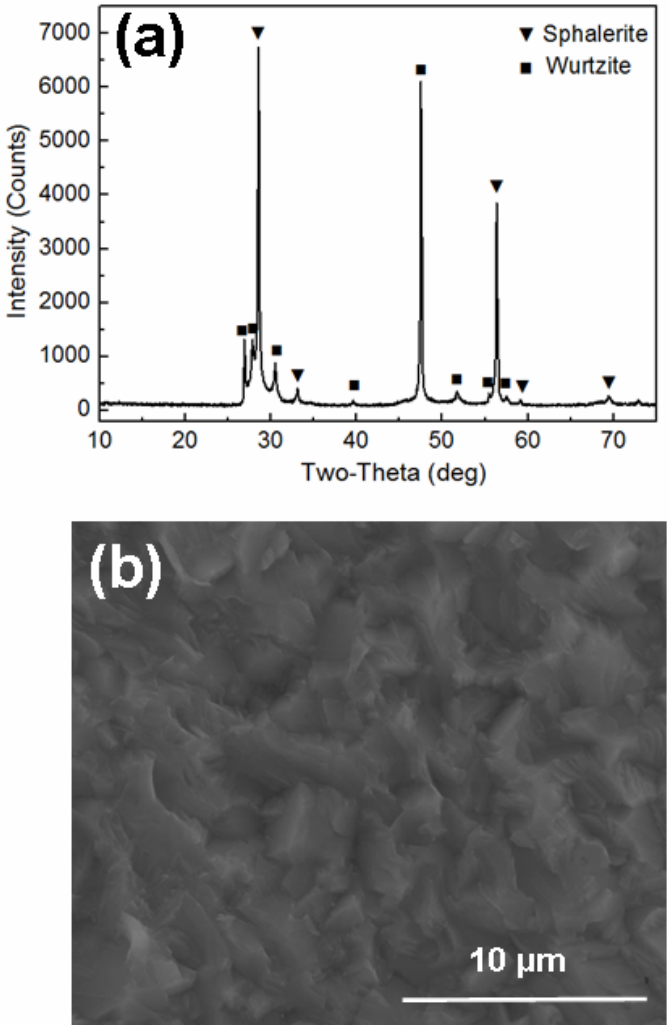

Figure 23. XRD pattern (a) and SEM micrograph (b) of the fracture surface for the as-sintered ZnS ceramics (Alfa & jet milled) by VHP.

The IR transmittance curve of the ZnS ceramic pellet (TAA & hot water bath) measured by FTIR is shown in Figure 24. It is characterized in the wavelength region from 2.5 μm to 25 μm for the sample sintered at 1000 ºC through VHP. It is found that

the maximum transmittance is around 77.3% at the wavelengths of 6.74 μm and 9.29 μm, which is desirable for applications in IR windows. It is observed that the peaks at 15.2 μm, 16.7 μm and 18.1 μm correspond to the Zn-S characteristic vibrations. The bands at 3.42 μm, 3.50 μm and 4.27 μm are due to the Zn-S microstructure formations. The peaks at 5.67-6.67 μm are attributed to the C=O stretching modes arising from CO_2 in the atmosphere.[81] According to photo image, the sample also obtains satisfactory transmittance in the visible region. The high transmittance is attributed to the high densification of ZnS ceramics thorough VHP of the colloidal processed (TAA & hot water bath) powders with good sintering properties. The large surface energy of the powders, the applied pressure and the vacuum condition serve as the driving forces to facilitate the consolidation process. It needs to be emphasized that the as-sintered ZnS ceramics might have slight carbon contamination leading to small peaks at 7.9 μm, 11.0 μm and 12.2 μm.[47] The light yellow color shown on the sample is assumed to result from the formation of defects during sintering.[51]

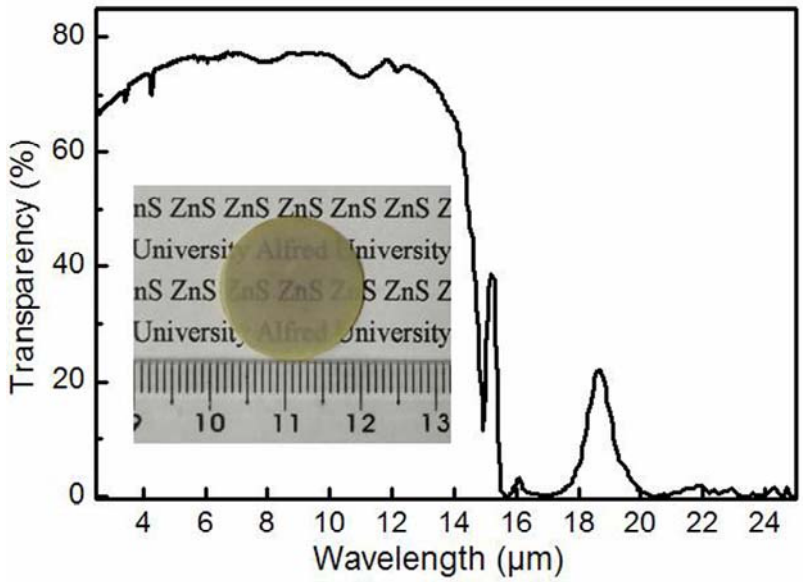

Figure 24. IR transmittance curve of the sintered ZnS ceramics (TAA & hot water bath) and the photo image of the ZnS ceramic pellet (inset) with a diameter of 18.75 mm and a thickness of 0.60 mm.

Figure 25 shows the IR transmittance curve of the sintered ZnS ceramics (Alfa

& jet milled). The maximum transmittance is 50.9% at around 11.9 μm. It has similar characteristic bands of Zn-S as the one for sintered ZnS ceramics (TAA & hot water bath). However, except the small similar carbon bands from penetration of graphite, there is a large absorption band at 9.6 μm corresponding to the C=C bond, which is derived from the presence of carbon. Since the sample sintered via FAST by using the same powders also has the same absorption band, it is assumed that the carbon might originate from the raw ZnS powders. Additionally, from the inset in the figure displaying the photo image, some dark dots within the sample also indicate the presence of carbon impurity. To sum up, by evaluating the optical properties of the ZnS ceramics sintered by both FAST and VHP, it is concluded that the synthesized ZnS powders (TAA & hot water bath) can lead to the as-sintered ZnS samples with best optical performance, due to their high purity, large specific surface area, and favorable morphology for sintering.

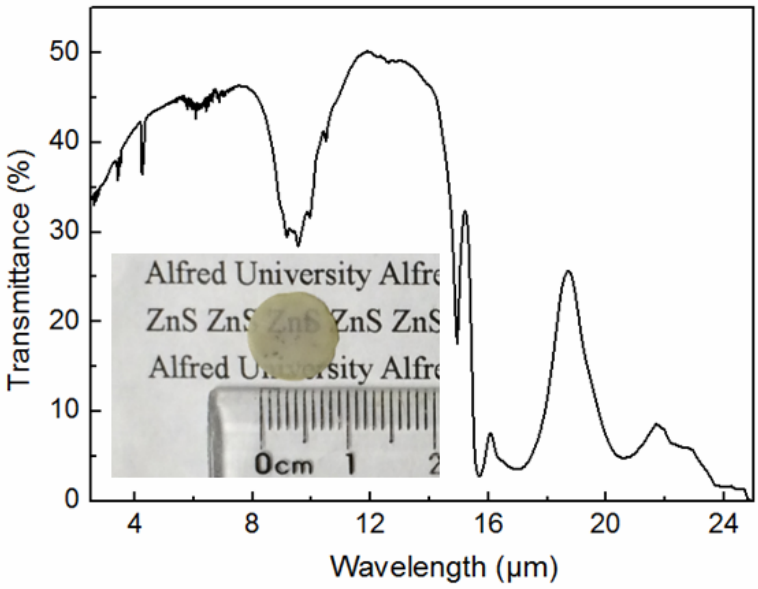

Figure 25. IR transmittance curve of the sintered ZnS ceramics (Alfa & jet milled) and the photo image of the ZnS ceramic pellet (inset) with a diameter of 10.00 mm and a thickness of 0.60 mm.

3. Comparison between FAST and VHP for Processing of ZnS Optical Ceramics

In this study, FAST and VHP sintering approaches were both applied to

consolidate ZnS powders. FAST employs pulsed direct current to enable high heating rate and short dwell time for densification at lower temperatures. VHP applies a vacuum condition in addition to the conventional hot pressing. By evaluating the results of the as-sintered ZnS ceramics by different sintering techniques, it is considered that the VHP is more suitable for fabricating the ZnS optical ceramics. The slower heating rate and loner dwell time can provide sufficient time and energy to rove the residual pores within ceramics during VHP process. Moreover, the slower loading of heat and pressure in VHP can be favorable of processing complete samples, rather than breaking samples into cracks in FAST with fast heating and pressure loading. In addition, the applied electric field loaded on the graphite dies and samples facilitate the penetration and contamination of highly conductive carbon into the ceramic compacts, resulting in deterioration of the optical transmittance.

4. Grain Growth Mechanism of ZnS Ceramics during VHP

The synthesized ZnS (TAA & hot water bath) powders were sintered at different temperatures by VHP to study the mechanism for grain growth in VHP process. The samples were sintered at 900 ºC, 950 ºC and 1000 ºC under a uniaxial pressure of 50 MPa for 2 hours. Figure 26 shows the XRD patterns of the samples. It is indicated that two phases exist within the samples, cubic sphalerite phase and hexagonal wurtzite phase. As can be observed from the comparison of the wurtzite peak (at 28 º) intensity between the three samples, with the increase of sintering temperature, more amounts of wurtzite are present in the ZnS ceramics, suggesting the phase transformation is proportionally temperature dependent.

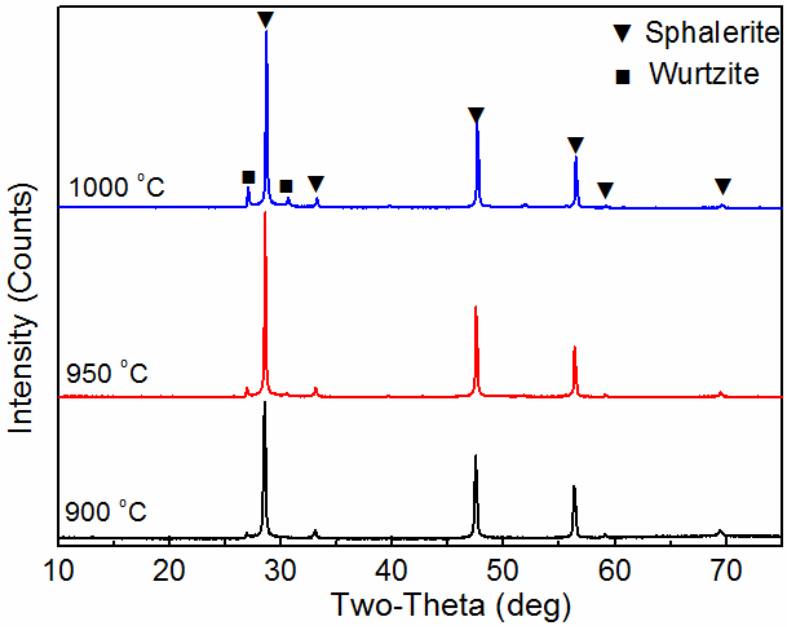

Figure 26. XRD patterns of the ZnS ceramics (TAA & hot water bath) sintered via VHP at 900 ºC, 950 ºC and 1000 ºC.

Figure 27 exhibits the IR transmittance curves of the ZnS ceramics (TAA & hot water bath) sintered at different temperatures. The photo images of the samples are shown in Figure 28. From both figures, it is indicated that the sample sintered at the higher temperature has better optical performance and higher density. Here, based on the previous results, it is considered that higher temperature is more favorable for the sufficient densification and pores removal of the ZnS ceramics, compared with the influence of presence of the second hexagonal phase.

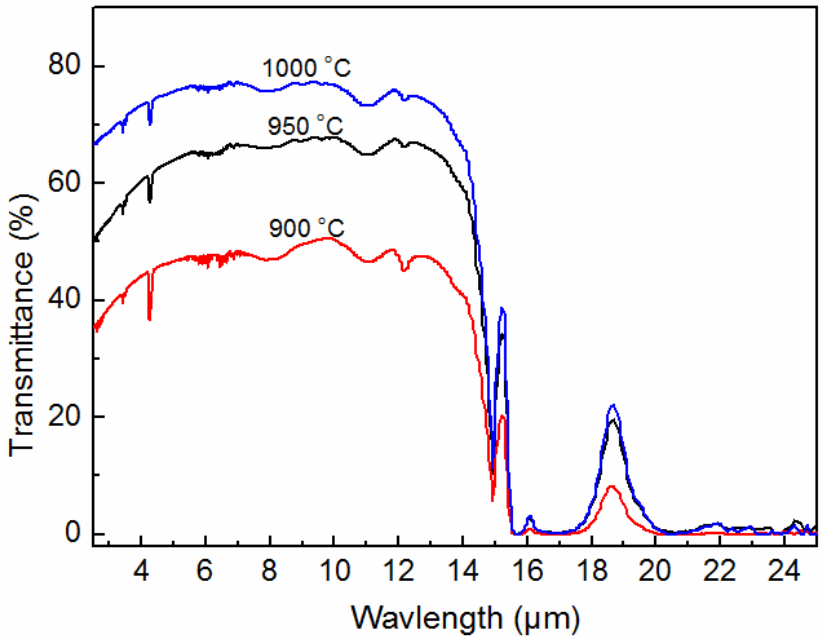

Figure 27. IR transmittance curves of the ZnS ceramics (TAA & hot water bath) sintered via VHP at 900 ºC, 950 ºC and 1000 ºC.

Figure 28. Photo images of the ZnS ceramics (TAA & hot water bath) sintered via VHP at 900 ºC (left), 950 ºC (middle) and 1000 ºC (right), with a diameter of 10.00 mm and a thickness of 0.60 mm.

The SEM images of the ZnS ceramics (TAA & hot water bath) sintered at different temperatures are displayed in Figure 29. As can be seen from the SEM images, the microstructure tends to be more densified as the sintering temperature

increases, which can explain the previous optical property improvement with the sintering temperature increase. Additionally, it is observed that the samples experience apparent grain growth from 900 ºC to 1000 ºC. The average grain sizes of the ZnS ceramics (TAA & Hot Water Bath) sintered at different temperatures (900 ºC, 950 ºC, and 1000 ºC) are measured to be 1.61 ± 0.38 μm, 2.68 ± 0.60 μm, and 3.14 ± 0.76 μm, respectively, which further confirms the grain growth. The grain growth is attributed to lattice diffusion, grain boundary diffusion, and Oswald ripening of ZnS grains.

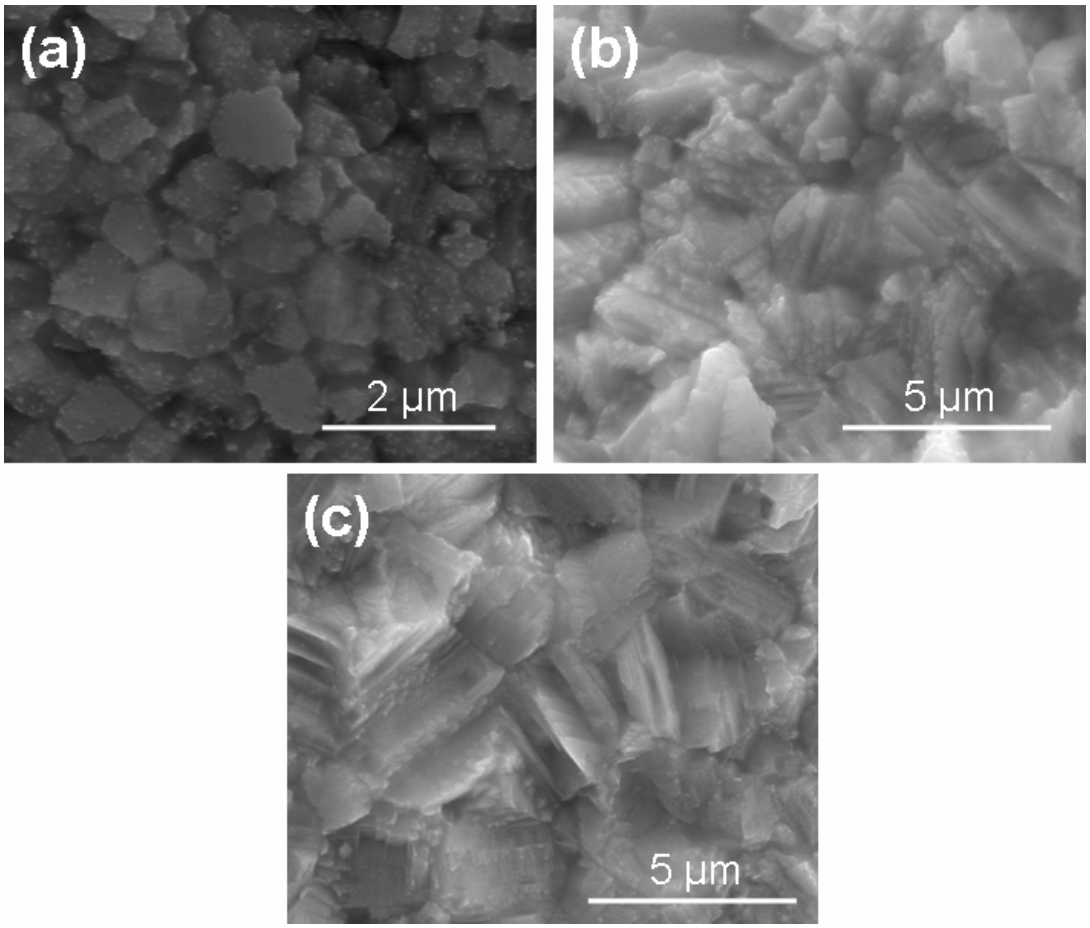

Figure 29. SEM images of the ZnS ceramics (TAA & hot water bath) sintered via VHP at 900 ºC (a), 950 ºC (b) and 1000 ºC (c).

The grain growth model can be predicted as a kinetic equation of the form as below:[82]

$$G^m - G_0^m = Kt \tag{13}$$

where G is the grain size at the time t, G_0 is the grain size at t=0, and K is a temperature-dependent rate constant obeying the Arrhenius equation as $K=A\exp(-Q/RT)$. Based on the Burke and Turnbull model, m=2 for the normal grain growth. Thus the equation can be changed as follows:

$$G^2 - G_0^2 = A\exp(-E_a / RT)t \tag{14}$$

$$\ln\frac{G^2 - G_0^2}{t} = \frac{-E_a}{RT} + \ln A \tag{15}$$

where G is the grain size at the time t, G_0 is the grain size at t=0, E_a is the activation energy for grain growth during densification, R is the gas constant, and T is the absolute temperature at which grains grow. From the analysis of SEM image of the raw synthesized ZnS powders, the average particle size is 0.17 μm. Therefore, the relationship between grain size and temperature during sintering of ZnS optical ceramics can be obtained in Figure 30. The activation energy for the grain growth is calculated from the slope to be 160.09 kJ/mol. This value is smaller than the reported activation energy during the HIP between 810 ºC and 980 ºC under 180 MPa, which was 150 kJ/mol.[52] The higher pressure from all directions of HIP can inhibit the lattice and grain boundary diffusions, leading to smaller activation energy. Since reports on the activation energy for ZnS optical ceramics are very few, and different ZnS raw powders contribute to different activation energies of grain growth for ZnS ceramics, it is difficult to make comparisons. Further study on activation energies of ZnS optical ceramics sintered by different ZnS raw powders will be conducted to compare different grain growth mechanisms during different sintering processes, such as FAST, VHP, pressureless sintering.

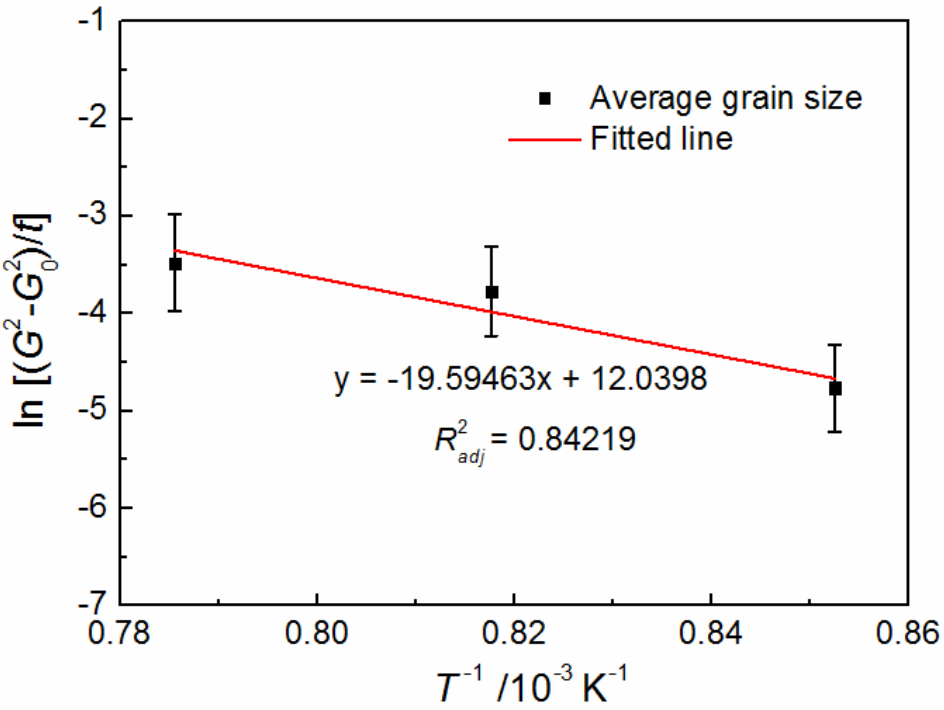

Figure 30. Relationship between grain size and temperature of the ZnS ceramics sintered by VHP.

D. Conclusions

To sum up, the present chapter studies the consolidation of ZnS optical ceramics via two pressure-assisted sintering approaches. It is demonstrated that the synthesized ZnS powders (TAA & hot water bath) can lead to as-sintered ZnS samples with best optical performance, due to their high purity, large specific surface area, and favorable morphology for sintering. Compared with FAST, VHP is a more favorable sintering approach for ZnS optical ceramics because of more sufficient consolidation and less carbon contamination. During the VHP process for ZnS optical ceramics (TAA & hot water bath), grain growth and densification occur at elevated temperatures. The grain growth of ZnS optical ceramics during densification in VHP is also briefly investigated and the activation energy is 160.09 kJ/mol.

PHOTOLUMINESCENCE OF ZNS OPTICAL CERAMICS

A. Introduction

The photoluminescence properties of doped and undoped nanostructured ZnS have extensively been studied. However, the reports on the photoluminescence characteristics of pressure-sintered ZnS ceramics were few. In this chapter, the photoluminescence characteristics of undoped ZnS ceramics sintered via FAST and VHP were investigated and studied. It was found that the undoped ZnS ceramics not only had the green photoluminescence properties but also long-lasting phosphorescence characteristics. Through characterizations on the phases, elements and optical characteristics, we intended to provide a rational discussion on the reason and mechanism for the photoluminescence.

B. Experimental Procedures

The ZnS powders synthesized by using Na_2S as the sulfur source were sintered via FAST, while the ZnS powders synthesized by using TAA via a hot water bath under acidic conditions were sintered via VHP. The synthesis methods and sintering profiles of the ZnS powders and as-sintered ZnS ceramics were mentioned in the previous parts. The phase composition of the ZnS powders and ceramics were measured via XRD (D2 PHASER, Bruker) equipped with a CuKα radiation (30 kV, 10 mA), with the measurement conditions of 10 to 75 º2θ, step size 0.02 º2θ and 0.3 second count time. The microstructures of the ZnS powders and as-sintered ceramics were investigated by environmental SEM (Quanta 200, FEI).

The ZnS ceramics sintered via FAST and VHP were also characterized to study photoluminescence performance and mechanism. The chemical elemental composition and valence of the ceramics were examined with wavelength dispersive spectroscopy (WDS, JEOL-JXA-8200, JEOL), X-ray photoelectron spectroscopy

(XPS, ESCALAB 250, Thermo Fisher) and X-ray fluorescence (XRF, Bruker S4 PIONEER). The characterization of photoluminescence (PL) was recorded using PL spectra (Jobin Yvon Fluorolog-3 spectrofluorometer, Horiba) and the phosphorescence property was confirmed by a compact fluorescence lifetime spectrometer (Quantaurus-Tau C11367, Hamamatsu Photonics) and a streak camera (C4434, Hamamatsu Photonics). All the characterizations of optical properties were at 300 K in air with an excitation wavelength of 365 nm.

C. Results and Discussion

1. Photoluminescence of the ZnS Ceramics via FAST

The XRD patterns of the synthesized ZnS powders and ceramic pellet sintered via FAST are shown in Figure 31. All the peaks in both synthesized powders and as-sintered ceramics patterns are well indexed as sphalerite (ICDD card no. 04-001-6857, F-43m, a = b = c = 5.40 Å). For the sintered ceramics, it is noteworthy that hexagonal wurtzite, the most commonly reported second phase detrimental to the optical properties of ZnS ceramics,[48] is not observed within the sample due to the relatively low sintering temperature of SPS. The sharper and narrower peaks can be explained by the grain growth during sintering including both the heating up process and dwelling process. From the SEM images shown in last chapter, it is shown that the ceramics are almost densified but some residual pores can still be observed.

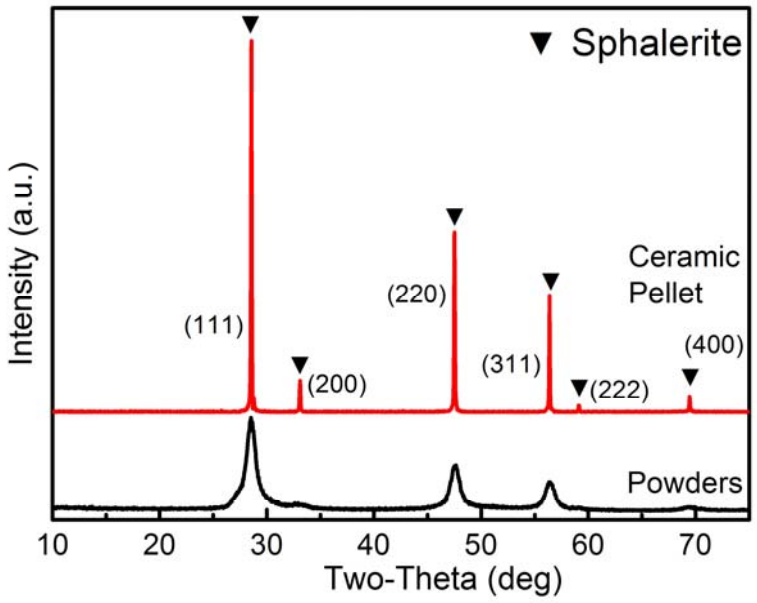

Figure 31. XRD patterns of the synthesized ZnS powders and ZnS sintered ceramics.

The qualitative elemental analysis of WDS for the ZnS ceramics is shown in Figure 32. The analysis was conducted by choosing six different areas in order to eliminate as many errors as possible. As can be seen from the figure, three main elements exist within the sample. Apart from the elements zinc and sulfur, a slight amount of carbon is detected in the ZnS ceramics, resulting from the carbon contamination during the SPS sintering process.[83] According to Table IV, showing the elements quantitative analysis of WDS of the sample (for zinc and sulfur), the atomic amount percent of sulfur is more than the one of zinc. It can be concluded that nonstoichiometry exists in the ZnS samples, which may be responsible for some imperfections in the crystallite. The excess of sulfur could result in zinc vacancies or sulfur interstitials in the ZnS crystals. Meanwhile, it may also lead to the excess of sulfur elemental species in the ZnS ceramics.

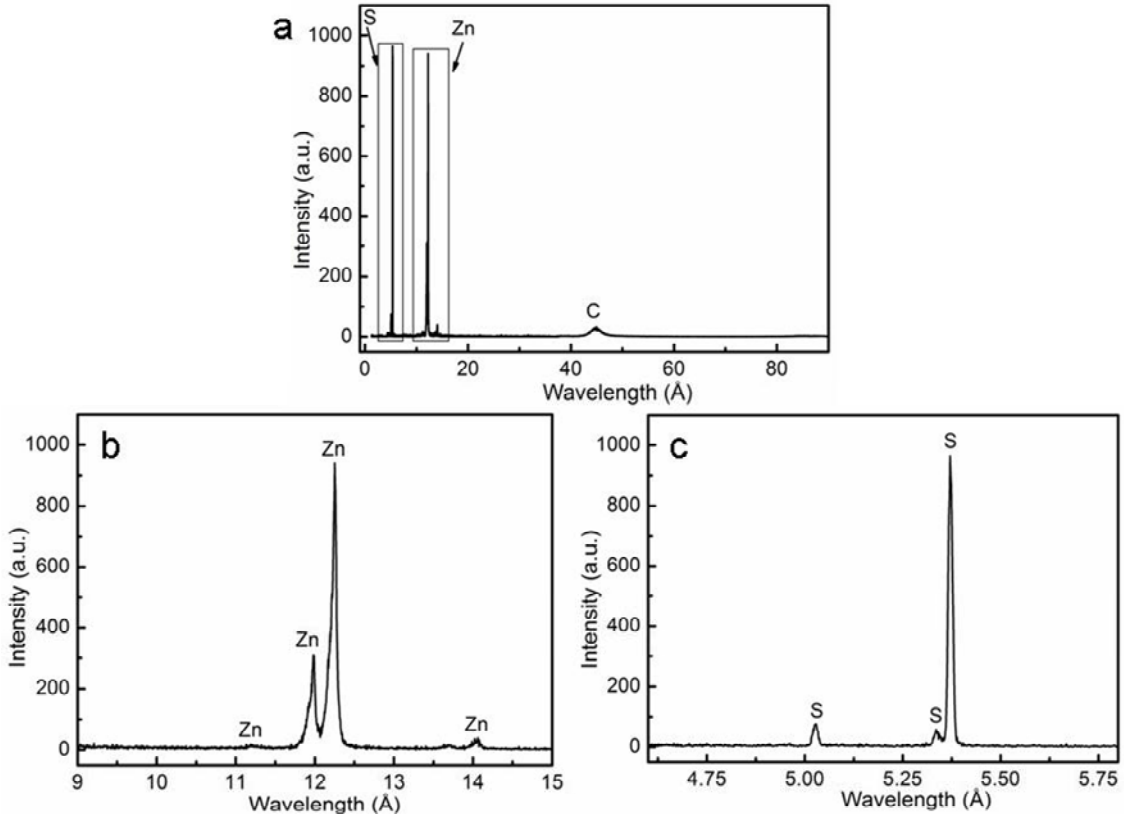

Figure 32. Elements qualitative analysis for the sintered ZnS ceramics by WDS ((a) corresponds to the whole spectrum, (b) to zinc and (c) to sulfur).

Table IV. Elements Quantitative Analysis of WDS of the Sintered ZnS Ceramics (For Sulfur and Zinc)

Elements	Mass (%)	Atom (%)
Sulfur	35.66	50.83
Zinc	64.34	49.17

Meanwhile, the elemental composition and valences of the elements zinc and sulfur within the sample were detected using XPS. It is shown that the major elements are sulfur and zinc, in accordance with the WDS results. Figure 33 indicates the valences of S and Zn investigated by XPS. It reveals that two peaks present in the zinc XPS graph. The low-energy peak at 1021.3 eV is due to Zn (2p 3/2) and the high-energy peak at 1044.3 eV corresponds to Zn (2p 1/2). Both peaks indicate that the valence of Zn in the sample is divalent and no other valences exist. In terms of

sulfur, the peak at 161.1 eV is due to the S^{2-} and the higher energy peak at 162.1 eV correlates with the elemental sulfur species on the surface of the sample.[84] It supports the assumption that the excess of sulfur results in the excess of elemental S species.

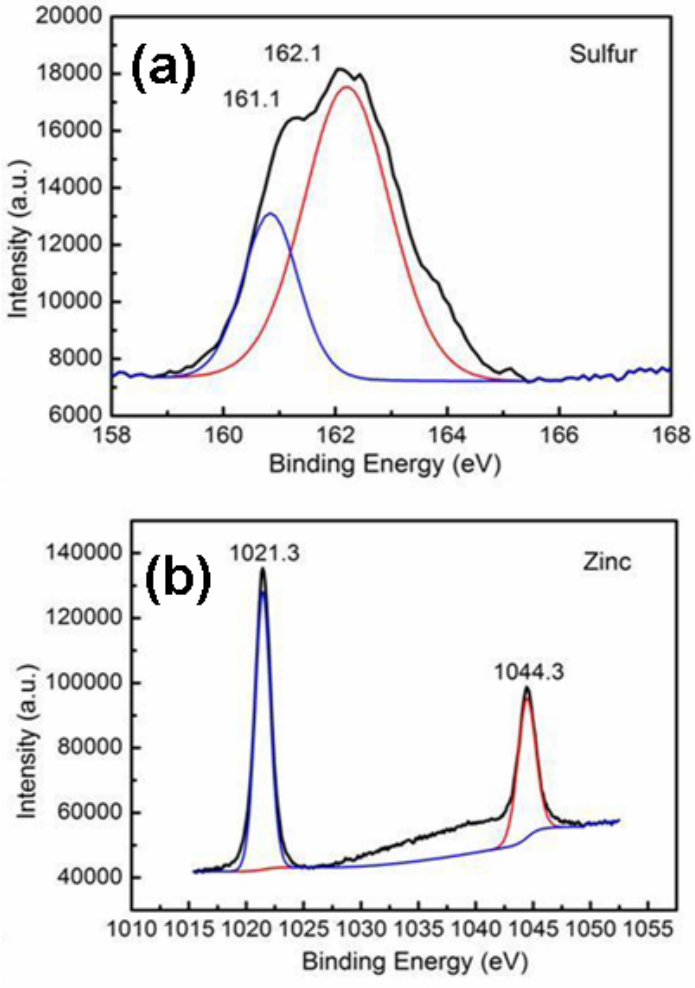

Figure 33. Valences of S (a) and Zn (b) for the ZnS ceramics investigated by XPS.

Figure 34 shows photos of the sintered ZnS ceramics. The pellet is in the diameter of 18.75 mm and in the thickness of 0.83 mm. UV lamp (ENF-280C, Spectroline, USA) was used to irradiate the ZnS ceramic pellet. It should be noted that the ceramic pellet exhibits the property of green photoluminescence in darkness without UV light irradiation, and it exhibits stronger green photoluminescence under UV light of wavelength 365 nm because of the higher energy of UV light than the one of visible light. Moreover, the green phosphorescence can still be clearly observed in darkness for more than 30 min.

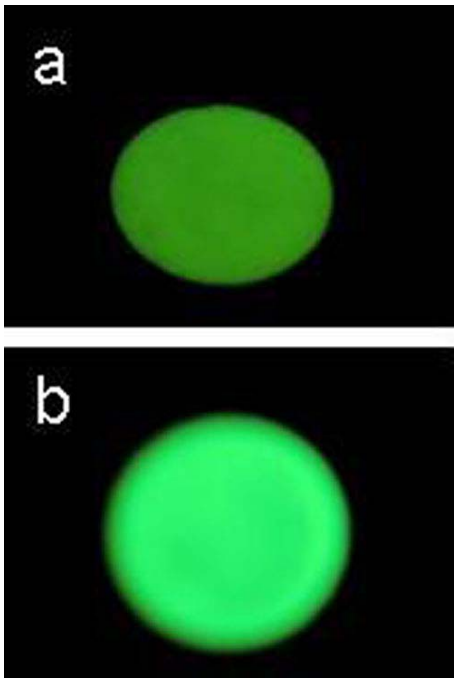

Figure 34. Photos of the ZnS ceramics in the darkness with UV light off (a) and the ZnS ceramics in the darkness with UV light on (b).

The PL spectra of the ZnS ceramics with green photoluminescence are illustrated in Figure 35. It can be observed that two emission peaks are detected within the sample. The weak peak at 460 nm is the indication of blue light and the strong peak at 530 nm is the indication of green light. The blue light may result from the self-activation of cation vacancies in the ZnS sample.[72,85] The strong green light, responsible for the green phosphorescence, is consistent with the ceramics observed in the aforementioned photos. It is should be noted that PL intensity for the peak at around 530 nm after UV light illumination is much weaker than the one before illumination, which results from the photo-oxidation process of elemental sulfur species on the surface of the ZnS ceramics. The detailed reason will be discussed in the following parts.

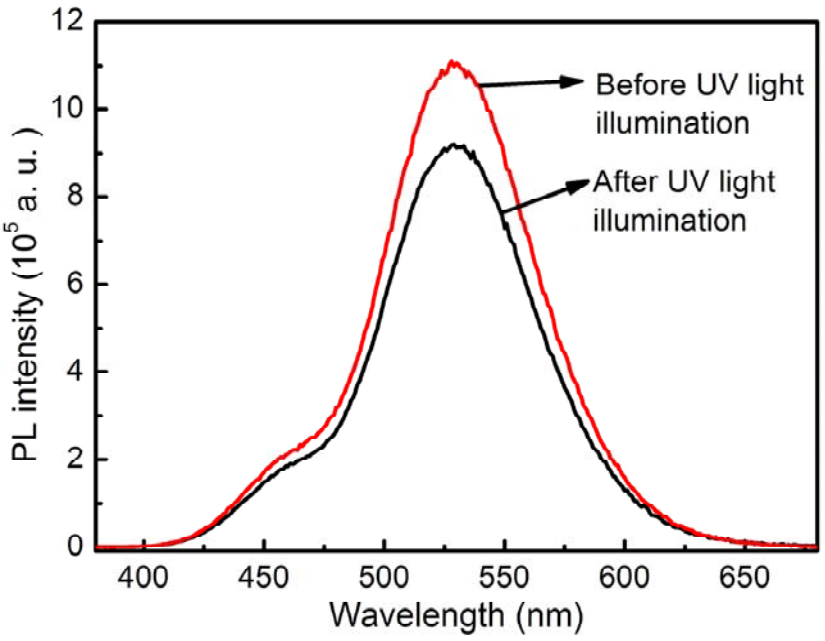

Figure 35. PL spectra of the ZnS ceramics measured at 300 K in air with an excitation wavelength of 365 nm (before UV light illumination and after 30 min UV light illumination).

Figure 36 displays the transient PL curve of the ZnS ceramics measured at 300 K in air with an excitation wavelength of 365 nm. The detection range of the fluorescence lifetime spectrometer is 50 μs-50 ms with a time resolution of 1 ns. The transient PL curve shown in Figure 36 is fitted by adopting 3rd order exponential decay fitting, and then the fluorescence lifetimes can be obtained. The fitted prompt lifetime τ_1 is 0.05 ms; the fitted delayed lifetimes τ_2 and τ_3 are 1.21 ms and 13.22 ms, respectively. As it indicates, prompt fluorescence and delayed fluorescence coexist in the sample. Compared with the prompt fluorescence, it can be clearly seen that the lifetime of delayed fluorescence corresponding to phosphorescence is much longer. In addition, the delayed fluorescence ratio (DR), determined by calculating the ratio for the addition of delayed lifetime multiplication with the corresponding decay constants and the total addition of lifetime multiplication with the corresponding decay constants, is calculated to be 97.8%, accounting for most of the luminescence of the sample. The delayed ratio is calculated by the equation:

$$DR(\%) = (\tau_2 A_2 + \tau_3 A_3) / (\tau_1 A_1 + \tau_2 A_2 + \tau_3 A_3) \times 100\% \quad (16)$$

where τ_1 corresponds to the fitted prompt lifetime; τ_2 and τ_3 correspond to the fitted delayed lifetimes; A_1, A_2 and A_3 are the corresponding decay constants for the lifetimes, respectively.

Moreover, the phosphorescence lifetime, in the unit of ms, exactly stands for the long afterglow property. The total photoluminescence quantum efficiency (PLQE) in the ZnS ceramic sample is determined by the ratio of the number of photons emitted and the one of photons absorbed obtained directly by the instrument. The total PLQE is measured to be 20%. According to the delayed ratio, the PLQE of the prompt component Φ_p and the PLQE of the delayed component Φ_d are calculated to be 19.56% and 0.44%, respectively.

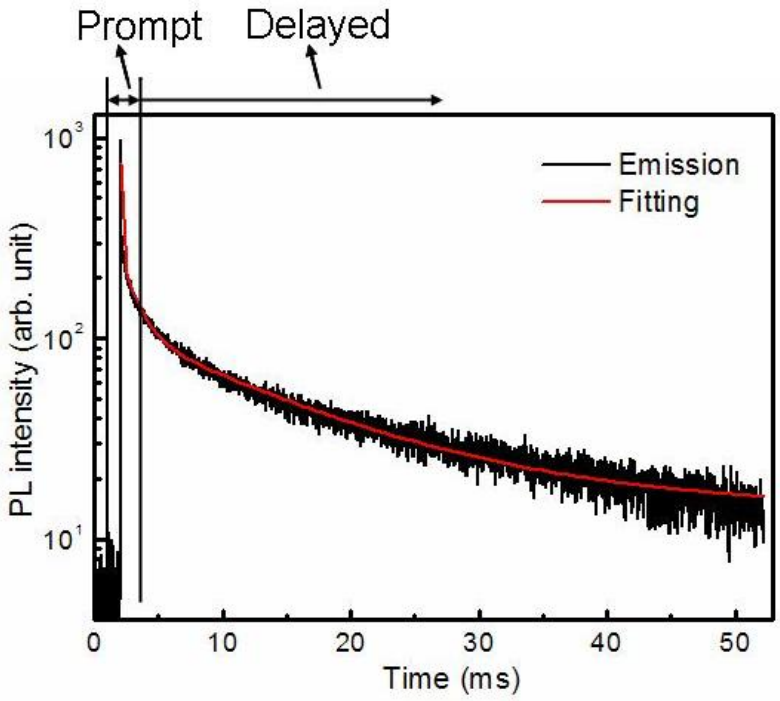

Figure 36. Transient PL curve of the ZnS ceramics measured at 300 K in air with an excitation wavelength of 365 nm.

The streak camera with a detection range of 0-10 ms and a time resolution of was employed in further confirming the green phosphorescence of the ZnS ceramics. Figure 37 shows the streak images and PL spectra of the ZnS ceramics for different time ranges of 10 μs, 500 μs and 10 ms. The measurement was taken with an excitation wavelength of 365 nm at 300 K. In the streak images, the spots correspond

to the intensity of photoluminescence: red, yellow, and green signal strong, intermediate and weak emission, respectively.[86] It can be seen from the images that the ZnS ceramics exhibit blue fluorescence (the peak at 460 nm) in the range of 10 μs. For 500 μs, both prompt blue fluorescence and green fluorescence (the peak at 530 nm) exist within the sample. As the time goes on to 10 ms, the green fluorescence is dominant and the peak for the blue fluorescence is weak. It should be noted that background of the streak image of 10 ms is attributed to delayed fluorescence of the ZnS ceramics. The PL spectra of the ZnS ceramics with different observation times are resolved and combined in Figure 38. It clearly further reveals that the blue fluorescence belongs to the prompt component and the green fluorescence belongs to the delayed component in the ZnS ceramics. Moreover, it can be seen that the PL spectrum with the time of 10 ms is very similar to the PL spectrum in Figure 38. Combined with all these aforementioned results, it can be concluded that the as-sintered ZnS ceramics have the characteristic of green phosphorescence.

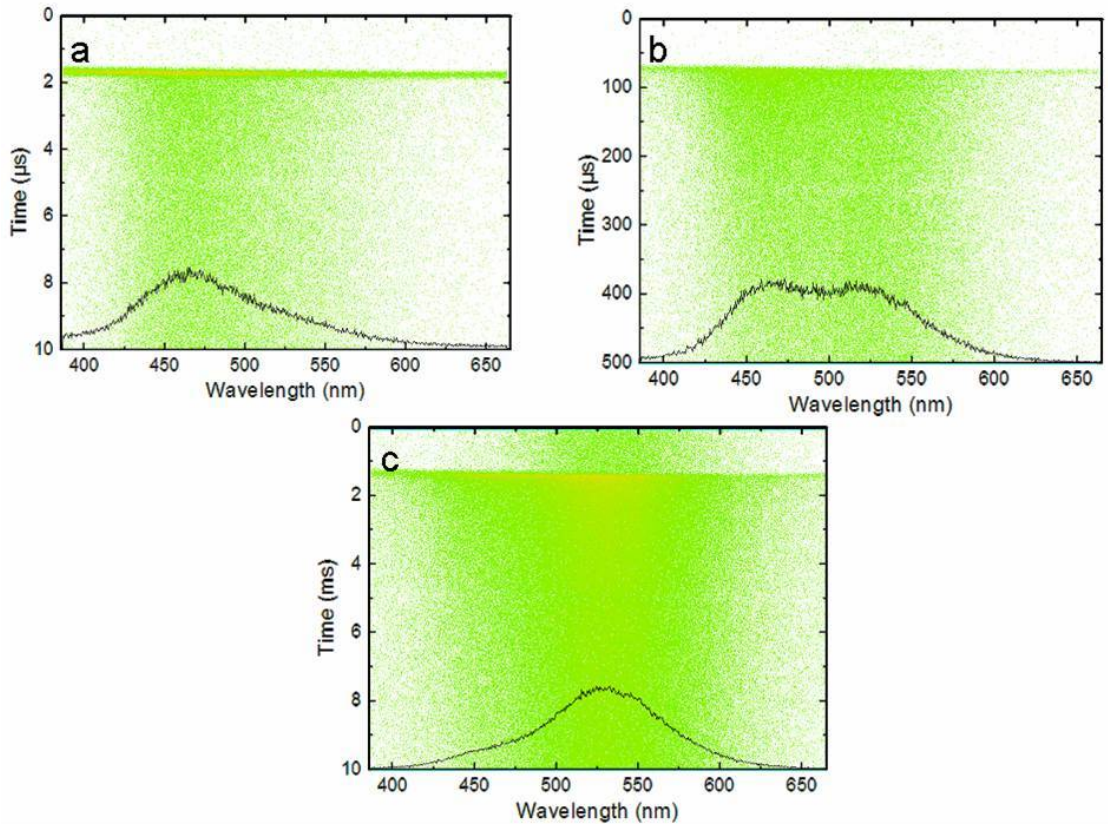

Figure 37. Streak images and PL spectra of the ZnS ceramics for different time ranges (a: 10 μs; b: 500 μs; c: 10 ms.)

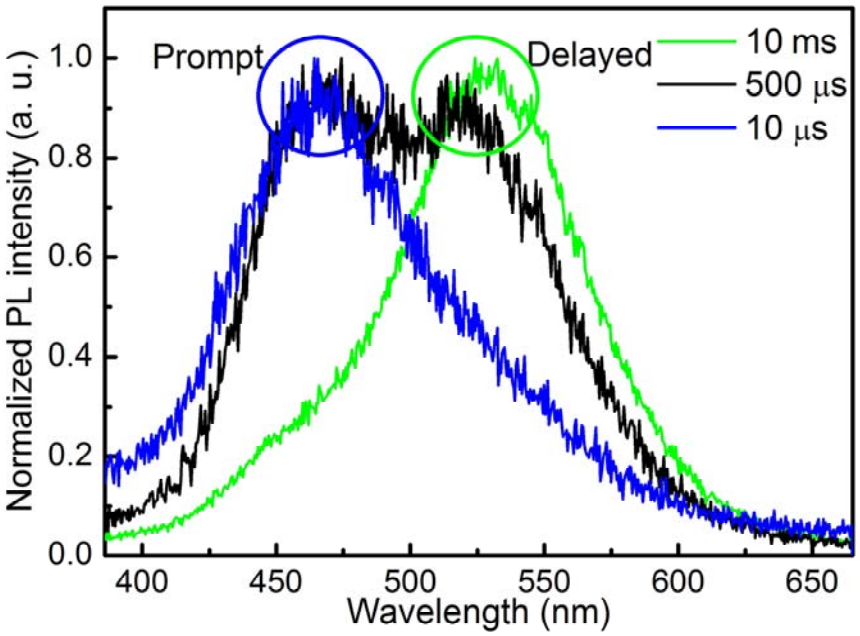

Figure 38. PL spectra of the ZnS ceramics with different observation times (10 μs, 500 μs and 10 ms) with an excitation wavelength of 365 nm.

The elemental analysis based on WDS and XPS mentioned above reveals and confirms the excess of elemental S species. It has been asserted in several references that the main reason for the green luminescence is the elemental sulfur species on the surface.[69,70,87] To confirm that the green luminescence is attributed to the excess of elemental sulfur species, the PL spectrum of the ZnS ceramics was measured after 30 min UV light illumination. Figure 35 shows the comparison of the PL spectra before and after UV light illumination. It reveals that the PL intensity for the peak at around 530 nm after UV light illumination is much weaker than the previous one. However, the peak for the blue light does not change very much. It is considered to be derived from the fact that UV light (almost 3-4 eV) is high enough to initiate the photo-oxidation process on the surface of ZnS sample and to transform elemental sulfur species to sulfur dioxides,[69,87] thus leading to the decrease of the PL intensity. PL intensity does recover after the irradiation of UV light because of the irreversible transformation of the elemental sulfur species to sulfur dioxides. In addition, it is

reported that the trapped electrons transfer on sulfur vacancies to sulfur interstitials states can also contribute to the green luminescence. Therefore, it is suggested that the transfer of sulfur defects associated with elemental sulfur species is responsible for the green luminescence. Given that WDS and XPS have the limitation of detection of the subsurface elements, XRF is adopted to detect the elemental composition for the whole ZnS ceramic pellets. From the semi-quantitative analysis of XRF, an additional small amount (less than 1%) of Na exists within the sample besides the main elements zinc and sulfur. Based on these results, we assume that it is the co-action of the transfer of sulfur defects associated with elemental sulfur species, and the imperfections in the ZnS crystals resulting from slight amounts of Na impurities from raw materials that facilitate the release of electromagnetic energy from triplet state to ground state and prolong the time for the green luminescence.[88-91] Further studies are needed to confirm the more detailed reasons of the phosphorescence.

2. Photoluminescence of the ZnS Ceramics via VHP

It is of interest to be noted that the as-sintered undoped ZnS ceramics by VHP also exhibit photoluminescence characteristics. Two emission bands at 450 nm and at 530 nm are obtained from the measured photoluminescence spectrum shown in Figure 39, corresponding to the blue color and green color, respectively. The blue emission band is reported be due to the electron transfer from Zn vacancies to conduction band.[72,92] It should be noted that the emission band wavelength has slight red shift compared with the sample sintered by FSAT. During the VHP process, phase transition occurs from sphalerite with a lower band gap to wurtzite with a higher band gap. Thus, the red shift is considered to be attributed the phase transition from sphalerite to wurtzite.[93]

Due to the much more intense peak at 530 nm, the sample displays strong green light under the UV light. In addition, the green luminescence can last long in darkness as shown in the inset picture, suggesting the phosphorescent characteristic of the as-sintered ZnS ceramics. It is assumed that the green emission results from the

transfer of the trapped electrons on sulfur vacancies to sulfur interstitials states accompanied by the elemental sulfur species on surface (as shown in Figure 40).[71,93] The ZnS powder synthesis and VHP sintering processes might enhance the lifetime of the green emission band. Further investigation needs to be performed on the mechanism of the luminescent properties of the sintered ZnS ceramics by VHP.

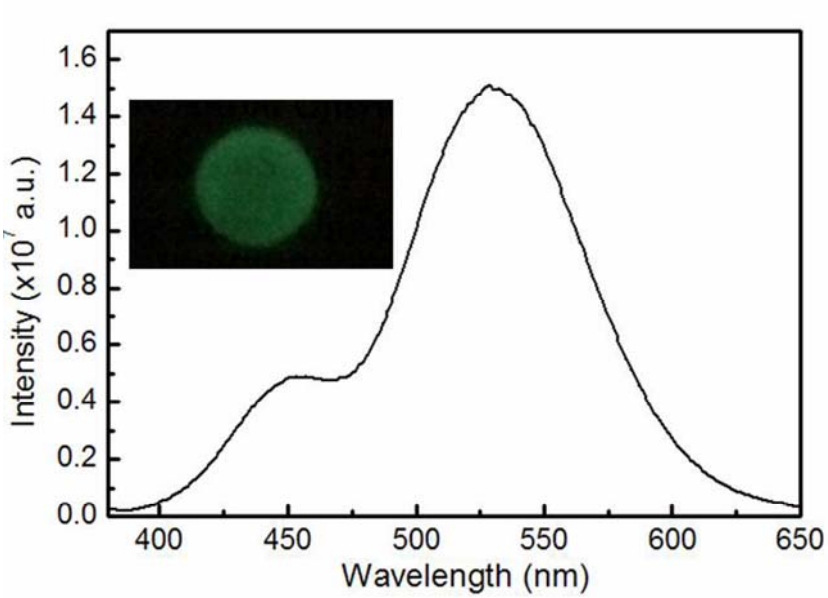

Figure 39. Photoluminescence emission spectrum for the sintered ZnS ceramics with an excitation wavelength of 365 nm and photo image of the ZnS ceramic pellet in darkness (inset).

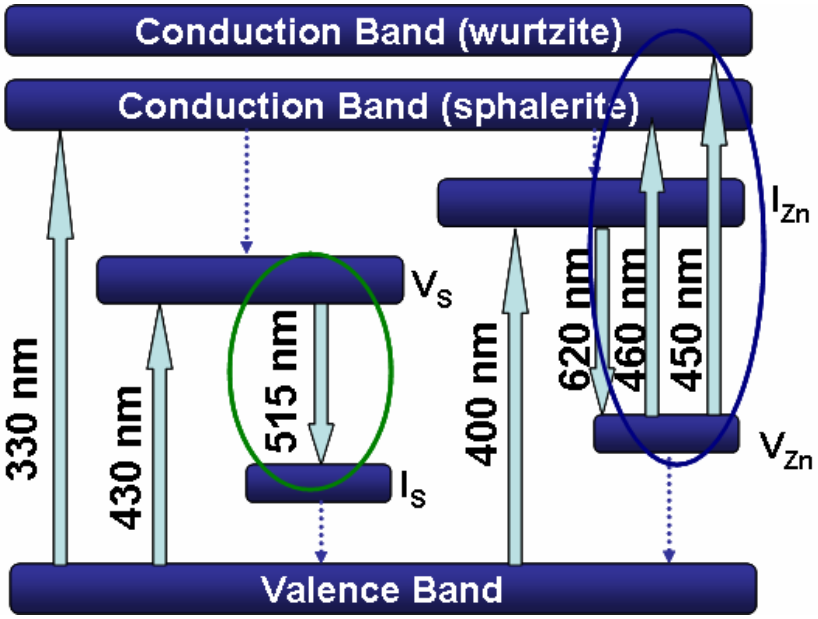

Figure 40. Schematic view of energy level diagram for the point defects in ZnS.[71,93]

D. Conclusions

Consolidated by FAST and VHP, the undoped ZnS optical ceramics are found exhibiting photoluminescence characteristics. In this chapter, the characteristics of blue and long lasting green photoluminescence of ZnS ceramics are confirmed. The blue emission band is thought to be due to the electron transfer from Zn vacancies to conduction band. It is also concluded that the green photoluminescence is derived from co-action of transfer of the trapped electrons on sulfur vacancies to sulfur interstitials states associated with elemental sulfur species on the surface. The increase of the luminescence lifetime is attributed to processing conditions. Further study and analysis will be needed to confirm the concrete reason of the long lasting green photoluminescence.

CONCLUSIONS

The present work reveals that all the synthesized ZnS powders have pure cubic ZnS sphalerite phase, while both commercial ZnS samples have the minor phase as hexagonal wurtzite. With small crystallites and particles, the synthesized ZnS powders are porous and have large specific surface area. Moreover, the colloidal processing and hot water bath can lead to the precipitation of homogeneous ZnS particles, due to the separation of controlled nucleation and particle growth.

The synthesized ZnS powders with spherical homogeneous particles lead to the consolidated ZnS ceramics with the best optical performance, due to their high purity, large specific surface area, and favorable morphology for sintering. Compared with FAST, VHP is a more favorable sintering approach for ZnS optical ceramics because of more sufficient consolidation and less carbon contamination. During the VHP process for ZnS optical ceramics, grain growth and densification occur at elevated temperatures and the activation energy for grain growth is 160.09 kJ/mol.

In addition, the as-sintered ZnS ceramics via both pressure-assisted sintering approaches were demonstrated to have photoluminescence characteristics. It is proposed that electron transfer sulfur defects associated with elemental sulfur species leads to the green luminescence. The increase of the luminescence lifetime is attributed to be related to processing conditions.

FUTURE WORK

This study is proposed to understand the relationship between processing and property for ZnS optical ceramics. In addition, it is performed to investigate the photoluminescence mechanism of ZnS optical ceramics. Based on the results of this work, the future study on ZnS optical ceramics can include:

1. Sintering mechanism for ZnS optical ceramics, including pressureless sintering, FAST and VHP.
2. Photoluminescence and application of ZnS optical ceramics doped with some transition metals and rare earth elements.
3. Kinetics for phase transition behavior of during sintering process of optical ZnS ceramics.

REFERENCES

1. W. D. Callister, *Fundamentals of Materials Science and Engineering*. John Wiley & Sons, Inc. , New York, 2001.

2. S. Wang, J. Zhang, D. Luo, F. Gu, D. Tang, Z. Dong, G. E. Tan, W. Que, T. Zhang, and S. Li, "Transparent Ceramics: Processing, Materials and Applications," *Prog. Solid State Chem.,* **41** [1] 20-54 (2013).

3. A. Krell, T. Hutzler, and J. Klimke, "Transmission Physics and Consequences for Materials Selection, Manufacturing, and Applications," *J. Eur. Ceram. Soc.,* **29** [2] 207-21 (2009).

4. A. Krell, J. Klimke, and T. Hutzler, "Transparent Compact Ceramics: Inherent Physical Issues," *Opt. Mater.,* **31** [8] 1144-50 (2009).

5. Y. Wu, "Nanostructured Transparent Ceramics with an Anisotropic Crystalline Structure," *Opt. Mater. Express,* **4** [10] 2026-31 (2014).

6. A. Ikesue, I. Furusato, and K. Kamata, "Fabrication of Polycrystal Line, Transparent YAG Ceramics by a Solid-State Reaction Method," *J. Am. Ceram. Soc.,* **78** [1] 225-8 (1995).

7. R. Chaim, R. Marder-Jaeckel, and J. Shen, "Transparent YAG Ceramics by Surface Softening of Nanoparticles in Spark Plasma Sintering," *Mater. Sci. Eng. A,* **429** [1] 74-8 (2006).

8. S. H. Lee, S. Kochawattana, G. L. Messing, J. Q. Dumm, G. Quarles, and V. Castillo, "Solid-State Reactive Sintering of Transparent Polycrystalline Nd:YAG Ceramics," *J. Am. Ceram. Soc.,* **89** [6] 1945-50 (2006).

9. T. Tachiwaki, M. Yoshinaka, K. Hirota, T. Ikegami, and O. Yamaguchi, "Novel Synthesis of $Y_3Al_5O_{12}$ (YAG) Leading to Transparent Ceramics," *Solid State Commun.,* **119** [10] 603-6 (2001).

10. I. Reimanis, H. Kleebe, R. Cook, and A. DiGiovanni, "Transparent Spinel Fabricated from Novel Powders: Synthesis, Microstructure and Optical Properties," DTIC Document, 2004.

11. K. Morita, B.-N. Kim, K. Hiraga, and H. Yoshida, "Fabrication of High-Strength Transparent $MgAl_2O_4$ Spinel Polycrystals by Optimizing Spark-Plasma-Sintering Conditions," *J. Mater. Res.,* **24** [09] 2863-72 (2009).

12. T. Lu, X. Chang, J. Qi, X. Luo, Q. Wei, S. Zhu, K. Sun, J. Lian, and L. Wang, "Low-Temperature High-Pressure Preparation of Transparent Nanocrystalline $MgAl_2O_4$ Ceramics," *Appl. Phys. Lett.,* **88** [21] 213120--3 (2006).

13. Y. Fang, D. Agrawal, G. Skandan, and M. Jain, "Fabrication of Translucent MgO Ceramics Using Nanopowders," *Mater. Lett.,* **58** [5] 551-4 (2004).

14. R. Chaim, Z. Shen, and M. Nygren, "Transparent Nanocrystalline MgO by Rapid and Low-Temperature Spark Plasma Sintering," *J. Mater. Res.,* **19** [09] 2527-31 (2004).

15. S. Dutta and G. Gazza, "Transparent Y_2O_3 by Hot-Pressing," *Mater. Res. Bull.,* **4** [11] 791-6 (1969).

16. H. Di, Y. Zheng, X. Sun, X. Li, and S. Liu, "Preparation of Transparent Y_2O_3 Ceramic by Slip Casting and Vacuum Sintering," *J. Rare Earth,* **30** [1] 57-62 (2012).

17. J. Wang, D. Chen, E. H. Jordan, and M. Gell, "Infrared-Transparent Y_2O_3-MgO Nanocomposites Using Sol-Gel Combustion Synthesized Powder," *J. Am. Ceram. Soc.,* **93** [11] 3535-8 (2010).

18. S. Xu, J. Li, C. Li, Y. Pan, and J. Guo, "Hot Pressing of Infrared-Transparent Y_2O_3-MgO Nanocomposites Using Sol-Gel Combustion Synthesized Powders," *J. Am. Ceram. Soc.,* (2014).

19. J. W. McCauley, P. Patel, M. Chen, G. Gilde, E. Strassburger, B. Paliwal, K. Ramesh, and D. P. Dandekar, "ALON: A Brief History of Its Emergence and Evolution," *J. Eur. Ceram. Soc.,* **29** [2] 223-36 (2009).

20. J. Cheng, D. Agrawal, Y. Zhang, and R. Roy, "Microwave Reactive Sintering to Fully Transparent Aluminum Oxynitride (ALON) Ceramics," *J. Mater. Sci. Lett.,* **20** [1] 77-9 (2001).

21. F. C. Sahin, H. E. Kanbur, and B. Apak, "Preparation of Alon Ceramics via Reactive Spark Plasma Sintering," *J. Eur. Ceram. Soc.,* **32** [4] 925-9 (2012).

22. K. Tsukuma, "Transparent Titania-Yttria-Zirconia Ceramics," *J. Mater. Sci. Lett.,* **5** [11] 1143-4 (1986).

23. U. Peuchert, Y. Okano, Y. Menke, S. Reichel, and A. Ikesue, "Transparent Cubic-ZrO_2 Ceramics for Application as Optical Lenses," *J. Eur. Ceram. Soc.,* **29** [2] 283-91 (2009).

24. H. Jiang, Y. Zou, Q. Chen, K. Li, R. Zhang, Y. Wang, H. Ming, and Z. Zheng, "Transparent Electro-Optic Ceramics and Devices," *Proc. SPIE*, **5644** 380-94 (2005).

25. W. Ruan, G. Li, J. Zeng, J. Bian, L. S. Kamzina, H. Zeng, L. Zheng, and A. Ding, "Large Electro-Optic Effect in La-Doped 0.75Pb $(Mg_{1/3}Nb_{2/3})O_3$-0.25$PbTiO_3$ Transparent Ceramic by Two-Stage Sintering," *J. Am. Ceram. Soc.,* **93** [8] 2128-31 (2010).

26. G. Wei, "Transparent Ceramics for Lighting," *J. Eur. Ceram. Soc.,* **29** [2] 237-44 (2009).

27. K. Hayashi, O. Kobayashi, S. Toyoda, and K. Morinaga, "Transmission Optical Properties of Polycrystalline Alumina with Submicron Grains," *Mater. Trans., JIM,* **32** [11] 1024-9 (1991).

28. X. Mao, S. Wang, S. Shimai, and J. Guo, "Transparent Polycrystalline Alumina Ceramics with Orientated Optical Axes," *J. Am. Ceram. Soc.,* **91** [10] 3431-3 (2008).

29. R. Apetz and M. P. Bruggen, "Transparent Alumina: A Light-Scattering Model," *J. Am. Ceram. Soc.,* **86** [3] 480-6 (2003).

30. S. Chen, Y. Wu, and Y. Yang, "Spark Plasma Sintering of Hexagonal Structure Yb^{3+}-Doped $Sr_5(PO_4)_3F$ Transparent Ceramics," *J. Am. Ceram. Soc.,* **96** [6] 1694-97 (2013).

31. M. Suárez, A. Fernández, J. L. Menéndez, and R. Torrecillas, "Sintering to Transparency of Polycrystalline Ceramic Materials"; pp. 527-52 in *Sintering of Ceramics - New Emerging Techniques.* Edited by Arunachalam Lakshmanan. InTech, Rijeka, Croatia, 2012.

32. Z. Liu, B. Mei, J. Song, and W. Li, "Optical Characterizations of Hot-Pressed Erbium-Doped Calcium Fluoride Transparent Ceramic," *J. Am. Ceram. Soc.,* **97** [8] 2506-10 (2014).

33. A. Ikesue and Y. L. Aung, "Ceramic Laser Materials," *Nature Photon.,* **2** [12] 721-7 (2008).

34. M. Tokita, "Mechanism of Spark Plasma Sintering," pp. 69-76 in *Proc. of the Inter. Sympo. on Microwave, Plasma and Thermochemical Processing of Advanced Materials, Osaka, Japan,* 1997.

35. X. R. Chen, X. F. Li, L. C. Cai, and J. Zhu, "Pressure Induced Phase Transition in ZnS," *Solid State Commun.,* **139** [5] 246-9 (2006).

36. Y. Zhou, A. J. Campbell, and D. L. Heinz, "Equations of State and Optical Properties of the High Pressure Phase of Zinc Sulfide," *J. Phys. Chem. Solids,* **52** [6] 821-5 (1991).

37. Y. Pan, S. Qu, S. Dong, Q. Cui, W. Zhang, X. Liu, J. Liu, B. Liu, C. Gao, and G. Zou, "An Investigation on the Pressure-Induced Phase Transition of Nanocrystalline ZnS," *J. Phys. Condens. Matter,* **14** [44] 10487 (2002).

38. A. Nazzal and A. Qteish, "Ab Initio Pseudopotential Study of the Structural Phase Transformations of ZnS under High Pressure," *Phys. Rev. B,* **53** [13] 8262 (1996).

39. C. Y. Yeh, Z. Lu, S. Froyen, and A. Zunger, "Zinc-Blende-Wurtzite Polytypism in Semiconductors," *Phys. Rev. B,* **46** [16] 10086 (1992).

40. X. S. Fang, T. Y. Zhai, U. K. Gautam, L. Li, L. M. Wu, Y. Bando, and D. Golberg, "ZnS Nanostructures: From Synthesis to Applications," *Prog. Mater. Sci.,* **56** [2] 175-287 (2011).

41. M. Catti, Y. Noel, and R. Dovesi, "Full Piezoelectric Tensors of Wurtzite and Zinc Blende ZnO and ZnS by First-Principles Calculations," *J. Phys. Chem. Solids,* **64** [11] 2183-90 (2003).

42. L. A. Xue and R. Raj, "Superplastic Deformation of Zinc Sulfide near Its Transformation Temperature [1020°]," *J. Am. Ceram. Soc.,* **72** [10] 1792-6 (1989).

43. Z. Wang, L. L. Daemen, Y. Zhao, C. Zha, R. T. Downs, X. Wang, Z. L. Wang, and R. J. Hemley, "Morphology-Tuned Wurtzite-Type ZnS Nanobelts," *Nature Mater.,* **4** [12] 922-7 (2005).

44. Y. Zhao, Y. Zhang, H. Zhu, G. C. Hadjipanayis, and J. Q. Xiao, "Low-Temperature Synthesis of Hexagonal (Wurtzite) ZnS Nanocrystals," *J. Am. Chem. Soc.,* **126** [22] 6874-5 (2004).

45. S. H. Yu and M. Yoshimura, "Shape and Phase Control of ZnS Nanocrystals: Template Fabrication of Wurtzite ZnS Single-Crystal Nanosheets and ZnO Flake-Like Dendrites from a Lamellar Molecular Precursor $ZnS{\cdot}(NH_2CH_2CH_2NH_2)_{0.5}$," *Adv. Mater.,* **14** [4] 296-300 (2002).

46. F. Huang, B. Gilbert, H. Zhang, and J. F. Banfield, "Reversible, Surface-Controlled Structure Transformation in Nanoparticles Induced by an Aggregation State," *Phys. Rev. Lett.,* **92** [15] 155501 (2004).

47. C. Chlique, O. Merdrignac-Conanec, N. Hakmeh, X. H. Zhang, and J. L. Adam, "Transparent ZnS Ceramics by Sintering of High Purity Monodisperse Nanopowders," *J. Am. Ceram. Soc.,* **96** [10] 3070-4 (2013).

48. L. A. Xue and R. Raj, "Effect of Hot-Pressing Temperature on the Optical Transmission of Zinc Sulfide," *Appl. Phys. Lett.,* **58** [5] 441-3 (1991).

49. D. C. Harris, "Development of Hot-Pressed and Chemical-Vapor-Deposited Zinc Sulfide and Zinc Selenide in the United States for Optical Windows," *Proc. SPIE*, **6545** 654502 (2007).

50. S. Chen and Y. Wu, "New Opportunities for Transparent Ceramics," *Am. Ceram. Soc. Bull.,* **92** [2] 32-7 (2013).

51. J. S. McCloy and R. W. Tustison, *Chemical Vapor Deposited Zinc Sulfide*. SPIE Press, Bellingham, 2013.

52. E. V. Karaksina, V. B. Ikonnikov, and E. M. Gavrishchuk, "Recrystallization Behavior of ZnS During Hot Isostatic Pressing," *Inorg. Mater.,* **43** [5] 452-4 (2007).

53. A. L. Chamberlain, W. G. Fahrenholtz, G. E. Hilmas, and D. T. Ellerby, "High-Strength Zirconium Diboride-Based Ceramics," *J. Am. Ceram. Soc.,* **87** [6] 1170-2 (2004).

54. V. Bheemineni, E. K. Chang, M. Lal, M. P. Harmer, and D. M. Smyth, "Suppression of Acceptor Solubilities in $BaTiO_3$ Densified in Highly Reducing Atmospheres," *J. Am. Ceram. Soc.,* **77** [12] 3173-6 (1994).

55. J. M. Huang, Y. Yang, S. H. Xue, B. Yang, S. Y. Liu, and J. C. Shen, "Photoluminescence and Electroluminescence of ZnS:Cu Nanocrystals in Polymeric Networks," *Appl. Phys. Lett.,* **70** [18] 2335-7 (1997).

56. G. Roussos and H. J. Schulz, "A New Emission of $ZnS:Ni^{2+}$ Arising from the 3T1(P)→3T1(F) Transition," *Solid State Commun.,* **51** [9] 663-4 (1984).

57. W. Chen, J. O. Malm, V. Zwiller, Y. N. Huang, S. M. Liu, R. Wallenberg, J. O. Bovin, and L. Samuelson, "Energy Structure and Fluorescence of Eu^{2+} in ZnS: Eu Nanoparticles," *Phys. Rev. B,* **61** [16] 11021-4 (2000).

58. J. F. Suyver, S. F. Wuister, J. J. Kelly, and A. Meijerink, "Synthesis and Photoluminescence of Nanocrystalline ZnS: Mn^{2+}," *Nano Lett.,* **1** [8] 429-33 (2001).

59. R. Sarkar, C. S. Tiwary, P. Kumbhakar, and A. K. Mitra, "Enhanced Visible Light Emission from Co^{2+} Doped ZnS Nanoparticles," *Physica. B,* **404** [21] 3855-8 (2009).

60. D. Amaranatha Reddy, G. Murali, R. P. Vijayalakshmi, B. K. Reddy, and B. Sreedhar, "Effect of Cr Doping on the Structural and Optical Properties of ZnS Nanoparticles," *Cryst. Res. Technol.,* **46** [7] 731-6 (2011).

61. S. Shionoya, T. Koda, K. Era, and H. Fujiwara, "Nature of Luminescence Transitions in ZnS Crystals," *J. Phys. Soc. Jpn.,* **19** 1157-67 (1964).

62. Y. Li, S. Zhou, Z. Chen, Y. Yang, N. Chen, and G. P. Du, "Luminescence Properties of Br-Doped ZnS Nanoparticles Synthesized by a Low Temperature Solid-State Reaction Method," *Ceram. Int.,* **39** [5] 5521-5 (2013).

63. C. Feldmann, T. Jüstel, C. Ronda, and P. Schmidt, "Inorganic Luminescent Materials: 100 Years of Research and Application," *Adv. Funct. Mater.,* **13** [7] 511-6 (2003).

64. D. A. Davies, J. Silver, A. Vecht, P. J. Marsh, and J. A. Rose, "A Novel Method for the Synthesis of ZnS for Use in the Preparation of Phosphors for CRT Devices," *J. Electrochem. Soc.,* **148** [10] H143-H8 (2001).

65. H. Hu and W. Zhang, "Synthesis and Properties of Transition Metals and Rare-Earth Metals Doped ZnS Nanoparticles," *Opt. Mater.,* **28** [5] 536-50 (2006).

66. M. Behboudnia and P. Sen, "Systematics in the Nanoparticle Band Gap of ZnS and $Zn_{1-X}M_xS$(M= Mn, Fe, Ni) for Various Dopant Concentrations," *Phys. Rev. B,* **63** [3] 035316 (2001).

67. R. N. Bhargava, D. Gallagher, X. Hong, and A. Nurmikko, "Optical Properties of Manganese-Doped Nanocrystals of ZnS," *Phys. Rev. Lett.,* **72** [3] 416 (1994).

68. T. Tsuruoka, C. H. Liang, K. Terabe, and T. Hasegawa, "Origin of Green Emission from ZnS Nanobelts as Revealed by Scanning near-Field Optical Microscopy," *Appl. Phys. Lett.,* **92** [9] 091908--3 (2008).

69. C. H. Ye, X. S. Fang, G. H. Li, and L. D. Zhang, "Origin of the Green Photoluminescence from Zinc Sulfide Nanobelts," *Appl. Phys. Lett.,* **85** [15] 3035-7 (2004).

70. C. H. Ye, X. S. Fang, M. Wang, and L. D. Zhang, "Temperature-Dependent Photoluminescence from Elemental Sulfur Species on ZnS Nanobelts," *J. Appl. Phys.,* **99** [6] 063504--4 (2006).

71. X. L. Wang, J. Y. Shi, Z. C. Feng, M. R. Li, and C. Li, "Visible Emission Characteristics from Different Defects of ZnS Nanocrystals," *Phys. Chem. Chem. Phys.,* **13** [10] 4715-23 (2011).

72. J. C. Lee and D. H. Park, "Self-Defects Properties of ZnS with Sintering Temperature," *Mater. Lett.,* **57** [19] 2872-8 (2003).

73. J. S. McCloy and B. G. Potter, "Photoluminescence in Chemical Vapor Deposited ZnS: Insight into Electronic Defects," *Optical Materials Express,* **3** [9] 1273-8 (2013).

74. H. P. Klug and L. E. Alexander, *X-Ray Diffraction Procedures: For Polycrystalline and Amorphous Materials,* Vol. 1. Wiley-Interscience, New York, 1974.

75. F. Zhang, "“Wet” Chemical Synthesis and Manipulation of Upconversion Nanoparticles"; pp. 21-71 in *Photon Upconversion Nanomaterials.* Springer, Berlin, Germany, 2015.

76. F. Huang and J. F. Banfield, "Size-Dependent Phase Transformation Kinetics in Nanocrystalline ZnS," *J. Am. Chem. Soc.,* **127** [12] 4523-9 (2005).

77. C. S. Tiwary, C. Srivastava, and P. Kumbhakar, "Onset of Sphalerite to Wurtzite Transformation in ZnS Nanoparticles," *J. Appl. Phys.,* **110** [3] 034908 (2011).

78. B. Gilbert, H. Zhang, F. Huang, M. P. Finnegan, G. A. Waychunas, and J. F. Banfield, "Special Phase Transformation and Crystal Growth Pathways Observed in Nanoparticles," *Geochem. Trans,* **4** [4] 20-7 (2003).

79. R. Dingreville, J. Qu, and M. Cherkaoui, "Surface Free Energy and Its Effect on the Elastic Behavior of Nano-Sized Particles, Wires and Films," *J. Mech. Phys. Solids,* **53** [8] 1827-54 (2005).

80. S. B. Qadri, E. F. Skelton, D. Hsu, A. D. Dinsmore, J. Yang, H. F. Gray, and B. R. Ratna, "Size-Induced Transition-Temperature Reduction in Nanoparticles of ZnS," *Phys. Rev. B,* **60** [13] 9191 (1999).

81. S. Ummartyotin, N. Bunnak, J. Juntaro, M. Sain, and H. Manuspiya, "Synthesis and Luminescence Properties of ZnS and Metal (Mn, Cu)-Doped-ZnS Ceramic Powder," *Solid State Sci.,* **14** [3] 299-304 (2012).

82. S. Somiya, *Handbook of Advanced Ceramics: Materials, Applications, Processing, and Properties*. Academic Press, Waltham, 2013.

83. C. Chlique, G. Delaizir, O. Merdrignac-Conanec, C. Roucau, M. Dollé, P. Rozier, V. Bouquet, and X. H. Zhang, "A Comparative Study of ZnS Powders Sintering by Hot Uniaxial Pressing (HUP) and Spark Plasma Sintering (SPS)," *Opt. Mater.,* **33** [5] 706-12 (2011).

84. D. E. Dunstan, A. Hagfeldt, M. Almgren, H. O. Siegbahn, and E. Mukhtar, "Importance of Surface Reactions in the Photochemistry of Zinc Sulfide Colloids," *J. Phys. Chem.,* **94** [17] 6797-804 (1990).

85. J. Prener and D. Weil, "The Luminescent Center in Self-Activated ZnS Phosphors," *J. Electrochem. Soc.,* **106** [5] 409-14 (1959).

86. A. Endo, K. Sato, K. Yoshimura, T. Kai, A. Kawada, H. Miyazaki, and C. Adachi, "Efficient up-Conversion of Triplet Excitons into a Singlet State and Its Application for Organic Light Emitting Diodes," *Appl. Phys. Lett.,* **98** 083302 (2011).

87. N. Kumbhojkar, V. V. Nikesh, A. Kshirsagar, and S. Mahamuni, "Photophysical Properties of ZnS Nanoclusters," *J. Appl. Phys.,* **88** [11] 6260-4 (2000).

88. K. Osada, "Phosphorescence of Sodium- and Potassium-Acetates," *J. Phys. Soc. Jpn.,* **11** [4] 425-9 (1956).

89. K. Osada, "Phosphorescence of Sodium Acetate," *J. Chem. Phys.,* **30** [5] 1363-4 (1959).

90. R. M. A. Von Wandruszka and R. J. Hurtubise, "Room-Temperature Phosphorescence of Compounds Adsorbed on Sodium Acetate," *Anal. Chem.,* **49** [14] 2164-9 (1977).

91. G. V. Colibaba, D. D. Nedeoglo, and V. V. Ursaki, "Impurity Centers in ZnSe: Na Crystals," *J. Lumin.,* **131** [9] 1966-70 (2011).

92. F. A. Kröger and H. J. Vink, "The Origin of the Fluorescence in Self-Activated ZnS, CdS, and ZnO," *J. Chem. Phys.,* **22** 250-2 (1954).

93. W. Zhang, X. H. Zeng, H. F. Liu, and J. F. Lu, "Synthesis and Investigation of Blue and Green Emissions of ZnS Ceramics," *J. Lumin.,* **134** 498-503 (2013).